Cellular/Molecular

Morphological Determinants of Cell-to-Cell Variations in Action Potential Dynamics in Substantia Nigra Dopaminergic Neurons

Estelle Moubarak, Yanis Inglebert, Fabien Tell,* and Jean-Marc Goaillard*
Unité Mixte de Recherche_S 1072, Aix Marseille Université, Institut National de la Santé et de la Recherche Médicale, Faculté de Médecine Secteur Nord, Marseille, France 13015

Action potential (AP) shape is a critical electrophysiological parameter, in particular because it strongly modulates neurotransmitter release. As it greatly varies between neuronal types, AP shape is also used to distinguish neuronal populations. For instance, AP duration ranges from hundreds of microseconds in cerebellar granule cells to 2-3 ms in SNc dopaminergic (DA) neurons. While most of this variation across cell types seems to arise from differences in the voltage- and calcium-gated ion channels expressed, a few studies suggested that dendritic morphology also affects AP shape. AP duration also displays significant variability in a same neuronal type, although the determinants of these variations are poorly known. Using electrophysiological recordings, morphological reconstructions, and realistic Hodgkin–Huxley modeling, we investigated the relationships between dendritic morphology and AP shape in rat SNc DA neurons from both sexes. In this neuronal type where the axon arises from an axon-bearing dendrite (ABD), the duration of the somatic AP could be predicted from a linear combination of the ABD and non-ABDs' complexities. Dendrotomy experiments and simulation showed that these correlations arise from the causal influence of dendritic topology on AP duration, due in particular to a high density of sodium channels in the somatodendritic compartment. Surprisingly, computational modeling suggested that this effect arises from the influence of sodium currents on the decaying phase of the AP. Consistent with previous findings, these results demonstrate that dendritic morphology plays a major role in defining the electrophysiological properties of SNc DA neurons and their cell-to-cell variations.

Key words: action potential; dendrites; dopamine; modeling; sodium channels; substantia nigra

Significance Statement

Action potential (AP) shape is a critical electrophysiological parameter, in particular because it strongly modulates neurotransmitter release. AP shape (e.g., duration) greatly varies between neuronal types but also within a same neuronal type. While differences in ion channel expression seem to explain most of AP shape variation across cell types, the determinants of cell-to-cell variations in a same neuronal type are mostly unknown. We used electrophysiological recordings, neuronal reconstruction, and modeling to show that, because of the presence of sodium channels in the somatodendritic compartment, a large part of cell-to-cell variations in somatic AP duration in substantia nigra pars compacta dopaminergic neurons is explained by variations in dendritic topology.

Received Nov. 25, 2021; revised June 22, 2022; accepted July 19, 2022.

Author contributions: F.T. and J.-M.G. designed research; E.M., Y.I., and F.T. performed research; E.M., F.T., and J.-M.G. analyzed data; E.M., F.T., and J.-M.G. wrote the manuscript.

This work was supported by French Ministry of Research Doctoral Fellowship to E.M.; and European Research Council Consolidator Grant 616827 *CanaloHmics* to J.-M.G. We thank Dr. Dominique Debanne for support with the confocal live imaging experiments.

The authors declare no competing financial interests.

*F.T. and J.-M.G. equally contributed to this work.

E. Moubarak's present address: School of Life Sciences, University of Sussex, Falmer, Brighton BN1 9QG, United Kingdom.

Y. Inglebert's present address: Department of Pharmacology and Therapeutics, McGill University, Montreal, Quebec H3A 1A3, Canada.

F. Tell and J.-M. Goaillard's present address: INT, Aix Marseille Université, Centre National de la Recherche Scientifique, Campus Santé Timone, Marseille, France 13005.

Correspondence should be addressed to Jean-Marc Goaillard at jean-marc.goaillard@univ-amu.fr or Fabien Tell at fabien.tell@univ-amu.fr.

https://doi.org/10.1523/JNEUROSCI.2331-21.2022

Copyright © 2022 the authors

Introduction

The diversity of neuronal types in the mammalian brain is associated with a significant variation in action potential (AP) shape, such that AP properties are sometimes used to distinguish between neighboring neuronal populations (Bean, 2007; Seutin and Engel, 2010; Bucher and Goaillard, 2011; Ding et al., 2011; Goaillard et al., 2020). In particular, AP duration (often defined by the width at half-amplitude or half-width) varies from 100 μs in rat cerebellum granule cells to 2-3 ms in substantia nigra pars compacta (SNc) dopaminergic (DA) neurons (Bean, 2007; Carter and Bean, 2009; Delvendahl and Hallermann, 2016; Moubarak et al., 2019; Goaillard et al., 2020). These variations in AP duration are often associated with differences in firing patterns: for instance, fast-spiking neurons tend to have short APs (submillisecond),

while cells with broad APs, such as DA or cholinergic neurons, tend to fire at lower frequencies (Lien and Jonas, 2003; Bean, 2007; Alle et al., 2009; Sengupta et al., 2010; Delvendahl and Hallermann, 2016). In addition, AP duration may vary in a same neuron, for instance, when the neuron is firing repeatedly at high frequency (Ma and Koester, 1996; Geiger and Jonas, 2000; Lien and Jonas, 2003), modifying in turn neurotransmitter release and the amplitude of synaptic responses in the postsynaptic neuron (Geiger and Jonas, 2000). From a mechanistic point of view, the density of ion channels underlying the upstroke and decay of the AP (in particular sodium and potassium channels), and the gating properties of the specific subunits expressed are partly responsible for the observed variation in AP duration (Bean, 2007; Alle et al., 2009; Carter and Bean, 2009, 2011; Sengupta et al., 2010; Seutin and Engel, 2010). For instance, the expression of specific subtypes of potassium channels (Kv3 and calcium-activated BK in particular) seems to be necessary to produce submillisecond APs (Rudy and McBain, 2001; Lien and Jonas, 2003; Bean, 2007; Alle et al., 2011; Kaczmarek and Zhang, 2017; Hunsberger and Mynlieff, 2020). While there is clear experimental evidence that the properties of sodium and potassium channels shape the AP, the influence of morphological parameters (axon to soma distance, dendritic morphology) on AP properties has been much less investigated. To date, only a few experimental studies and mostly theoretical studies have suggested that differences in morphology may also play a role in the variation of AP duration across neuronal types (Vetter et al., 2001; Kuba et al., 2005; Brette, 2013; Eyal et al., 2014; Gulledge and Bravo, 2016; Kole and Brette, 2018; Goaillard et al., 2020). In addition, the influence of cell-to-cell variations in morphology on AP properties in a same neuronal type has never been investigated experimentally.

In SNc DA neurons, the axon most often arises from an axon-bearing dendrite (ABD) at distances as far as 200 µm from the soma (Hausser et al., 1995; Gentet and Williams, 2007; Meza et al., 2018; Moubarak et al., 2019). The AP, initiated at the axon initial segment (AIS), is faithfully back-propagated by the progressive recruitment of somatodendritic (SD) sodium channels (Hausser et al., 1995; Gentet and Williams, 2007; Seutin and Engel, 2010; Moubarak et al., 2019). In this context, we wondered whether the shape of the AP recorded at the soma and its back-propagation efficiency were influenced by the specific morphologies of the ABD and the non-axon bearing dendrites (nABDs). Using somatic recordings from 38 fully reconstructed neurons, we found that AP HW could be predicted from a linear combination of the respective complexities of the ABD and nABDs (negatively and positively correlated, respectively). The opposite influence of ABD and nABDs was confirmed by selective dendrotomy experiments. Using realistic multicompartment Hodgkin–Huxley modeling, we then demonstrated that dendritic topology predicts AP HW only when the ABD contains more sodium and/or calcium channels than the nABDs, and that this relationship surprisingly arises from the influence of sodium currents on the decaying phase of the AP. In line with previous findings (Moubarak et al., 2019), these results demonstrate that dendritic morphology plays a major role in defining the electrophysiological properties of SNc DA neurons, such that specific cell-to-cell variations in AP dynamics appear to result mainly from variations in dendritic topology.

Materials and Methods

The dataset of neurons presented in this article is the same that was used in a recent publication (Moubarak et al., 2019). Additional electrophysiological and morphological parameters, not analyzed for the first article, were extracted from this dataset to perform the current study. Moreover, dendrotomy experiments and new modeling simulations were specifically performed for the current study.

Acute midbrain slice preparation. Acute slices were prepared from P19-P21 (mean = P20) Wistar rats of either sex ($n = 19$). All experiments were performed according to the European (Council Directive 86/609/EEC) and institutional guidelines for the care and use of laboratory animals (French National Research Council). Rats were anesthetized with isoflurane (CSP) in an oxygenated chamber (TEM SEGA) and decapitated. The brain was immersed briefly in oxygenated ice-cold low-calcium aCSF containing the following (in mM): 125 NaCl, 25 $NaHCO_3$, 2.5 KCl, 1.25 NaH_2PO_4, 0.5 $CaCl_2$, 4 $MgCl_2$, 25 D-glucose; or 87 NaCl, 25 $NaHCO_3$, 2.5 KCl, 1.25 NaH_2PO_4, 0.5 $CaCl_2$, 7 $MgCl_2$, 10 D-glucose, 75 sucrose; pH 7.4, oxygenated with 95% O_2/5% CO_2 gas. The cortices were removed, and then coronal midbrain slices (250 or 300 μm) were cut on a vibratome (Leica VT 1200 or 1200S) in oxygenated ice-cold low calcium aCSF. Following 20-30 min incubation in 32°C oxygenated low calcium aCSF, the slices were incubated for at least 30 min in oxygenated aCSF (125 NaCl, 25 $NaHCO_3$, 2.5 KCl, 1.25 NaH_2PO_4, 2 $CaCl_2$, 2 $MgCl_2$, and 25 glucose, pH 7.4, oxygenated with 95% O_2 5% CO_2 gas) at room temperature before electrophysiological recordings.

Drugs. Picrotoxin (100 μM, Sigma Aldrich) and kynurenate (2 mM, Sigma Aldrich) were bath-applied via continuous perfusion in aCSF to block inhibitory and excitatory synaptic activity, respectively.

Electrophysiology recordings and analysis. All recordings (45 cells from 19 rats) were performed on midbrain slices continuously superfused with oxygenated aCSF. Patch pipettes (1.8-3 MOhm) were pulled from borosilicate glass (GC150TF-10, Havard Apparatus) on a DMZ Universal Puller (Zeitz Instruments). The patch solution contained the following (in mM): 20 KCl, 10 HEPES, 10 EGTA, 2 $MgCl_2$, 2 Na-ATP, and 120 K-gluconate, pH 7.4, 290-300 mOsm. Neurobiotin (0.05%; Vector Labs) was included in the intracellular solution to allow morphological reconstruction and identification of dopaminergic neurons using *post hoc* TH immunolabeling (Amendola et al., 2012; Moubarak et al., 2019). Whole-cell recordings were made from SNc DA neurons visualized using infrared differential interference contrast videomicroscopy (QImaging Retiga camera; Olympus BX51WI microscope) and identified as previously described (Amendola et al., 2012; Moubarak et al., 2019). Whole-cell current-clamp recordings with a series resistance <10 MOhm were included in the study. Capacitive currents and liquid junction potential (13.2 mV) were compensated online, and offset potentials were measured after removing the pipette from the neuron. Bridge balance (100%, 10 µs) was used to compensate series resistance. Recordings with offset values >1 mV were discarded from the analysis. Recordings were acquired at 50 kHz and were filtered with a low-pass filter (Bessel characteristic between 2.9 and 5 kHz cutoff frequency). APs generated during a 40 s period of spontaneous activity were averaged and the AP threshold, AP amplitude, and the duration of the AP at half of the maximal height of the AP (AP half-width, AP HW) were measured. AP threshold was measured on the d^2v/dt^2 versus V phase plane plot.

Laser photo-ablation of dendrites. For dendrotomy experiments, Alexa-594 (4%, Invitrogen) and neurobiotin (0.05%, Vector Labs) were included in the patch solution, and confocal live imaging was performed on an LSM 710 Zeiss confocal microscope (Carl Zeiss), with the images being captured using Zeiss ZEN software. Recordings and live imaging were started 10-15 min after obtaining the whole-cell configuration to allow substantial diffusion of the dye into the dendritic tree. To prevent fatal damage of the neuron, an ROI was then chosen on a secondary or tertiary dendrite, at least 50 µm from the soma. A *z*-stack image of the neuron comprising the ROI and the soma was taken before starting the laser photo-ablation procedure. The ROI was then illuminated for 10-15 s with medium power using a 543 nm laser. After a 1-5 min recovery period, images of the ROI were taken to assess ablation success. Dendrotomy is characterized by

Table 1. Equations governing the voltage dependence and kinetics of currents in the model[a]

Current general equations (except for I_{SK})

$$I(V,t) = g_{max} \times m^a(V,t) \times h^b(V,t) \times (V - E_{rev})$$

$$m_\infty(V) = \frac{1}{\left(1+exp\left[\left(\frac{-(V - V_m)}{k_m}\right)\right]\right)} \qquad h_\infty(V) = \frac{1}{\left(1+exp\left[\left(\frac{-(V - V_h)}{k_h}\right)\right]\right)} \qquad dt = 20\ \mu s$$

$$dm(V,t)/dt = \frac{\left[m_\infty(V) - m(V,t)\right]}{\tau_m} \qquad dh(V,t)/dt = \frac{\left[h_\infty(V) - h(V,t)\right]}{\tau_h}$$

Current	V_m mV	k_m mV	a	V_h mV	k_h mV	b	E_{rev} mV	Specific equations (τ_m and τ_h are expressed in ms)	g_{max} (pS/μm^2) Soma/nABDs	ABD	AIS	axon
I_{Na}	−28	8	3	−50	−10	1	60	$\tau_m = 0.01+(0.33/(1+((V+20)/30)^2))$ $\tau_h = 0.7+(16/(1+((V+50)/8)^2))$	75 50	75-165 (#1, #2) 50-150 (#3, #4)	4000	400
I_{KDR}	−30	9	4	-	-	0	−90	τ_m =(4* exp(-(0.000729)*((V +32)^2))) + 4	150	150 or 50 (#6)	4000	400
I_A	−30 (soma) −35 (dendrite)	7	1	−75 (soma) −85 (dendrite)	−7	1	−90	τ_m =1.029 + (4.83/(1+exp((V + 57)/6.22))) τ_h = 25+ (50+(78.4/(1+exp(V + 68.5)/5.95)) −25)/(1+exp((-V-80)*5))	100 (nABDs) 150 (soma)	100	0	0
I_H	−92	−7.25	1	-	-	0	−40	τ_m = 556 + 1100*exp(−0.5*((V)/11.06)^2)	0.5	0.5 or 2 (#5)	0	0
I_{CaL}	−31	7	1	-	-	0	120	τ_m = 1/((−0.209*(V + 39.26) /(exp(-(V + 39.26)/4.111)−1)+ (0.944*exp(-(V + 15.38)/224.1))))	1	1-3	0	0
I_{SK}	-	-	-	-	-	-	−90	$I(V, Ca_i) = g_{max} \times O_\infty(Ca_i) \times (V - E_{rev})$ $O_\infty(V) = (Ca_i)^4/((Ca_i)^4 + (0.00019)^4)$	0.1	0.1	0	0

Calcium buffering and pump (see Destexhe et al., 1993)

[a]The six versions of the model implementing different values of g_{Na}, g_{KDR}, g_H, or g_{CaL} in the ABD are indicated (#) with the corresponding conductance values or ranges.

membrane swelling in the ROI and loss of upstream and downstream fluorescence (Go et al., 2016; Rama et al., 2017). The illumination procedure was repeated as many times as necessary until ablation was achieved. After dendrotomy was obtained, a *z*-stack image of the neuron comprising the ROI and the soma was taken, and compared with the image taken before laser illumination. APs were induced by incremental step current injections and recorded before and after each laser illumination.

Electrophysiology data acquisition and analysis. Data were acquired with a HEKA EPC 10/USB patch-clamp amplifier (HEKA Electronics) and patchmaster software (HEKA Electronics) or a Multiclamp 700B (Molecular Devices). Analysis was conducted using FitMaster v2x30 (Heka Elektronik) and Clampfit (Molecular Devices).

Immunohistochemistry and morphological reconstruction. Acute slices containing Neurobiotin-filled cells were fixed 30 min in 4% PFA at 4°C and immunolabelled with anti-TH (chicken polyclonal, Abcam, 1:1000) and anti-AnkyrinG (mouse monoclonal IgG2b, NeuroMab, 1:250) antibodies. Goat anti-mouse IgG2b AlexaFluor-488 (Invitrogen; 1:1000; 2 μg/ml) and goat anti-chicken AlexaFluor-633 (Invitrogen; 1:3000; 1.66 ng/ml) were used to reveal TH and AnkyrinG stainings, respectively. Streptavidin AlexaFluor-594 (Invitrogen; 1:12000; 1.66 ng/ml) was used to reveal neurobiotin labeling. Slices were mounted in Faramount mounting medium (Dako). Immunolabelings were viewed on an LSM 780 Zeiss (Carl Zeiss), and images were captured using Zeiss ZEN software. Images were analyzed with Fiji/ImageJ software (Schindelin et al., 2012; Schneider et al., 2012; Rueden et al., 2017); and in particular, neurons were reconstructed using the Simple Neurite Tracer plugin (Longair et al., 2011). The axon was identified using ankyrinG labeling, which allowed us to discriminate between ABD and nABDs. All dendritic lengths were extracted directly from the paths traced through the stack images of the neurons, this measure corresponding to the sum of the lengths of all dendritic segments arising from a given primary dendrite (ABD or nABD). To assess dendritic complexity, we extracted from the reconstructions the number of dendritic segments (branches) found on the ABD and nABDs. The average length and number of segments per nABD were obtained by dividing the total for these parameters by the number of primary nABD dendrites for each neuron. Soma volumes were estimated by using the "fill out path" method on Simple Neurite Tracer. For the diameters of the primary dendrites, intermediate ABD dendrites, axon, and AIS, the fluorescence histograms of branch sections were obtained and fitted with a Gaussian curve model. Diameters were then estimated as 3 × SD of the Gaussian distribution.

Multicompartment modeling. Simulations were performed using NEURON 7.5 software (Hines and Carnevale, 1997, 2001; Carnevale and Hines, 2005), as described in a previous publication (Moubarak et al., 2019). Neuronal morphologies correspond to the realistic morphologies from the 37 fully reconstructed dopaminergic neurons.

For each compartment, membrane voltage was obtained as the time integral of a first-order differential equation:

$$\frac{dV}{dt} = \frac{-1}{C_m} * \sum \left[g_i * (V_m - V_{rev})\right] - I_{axial}$$

where V_m is the membrane potential, C_m the membrane capacitance, g_i are ionic conductances, and V_{rev} their respective reversal potentials. The axial flow of current (I axial) between adjacent compartments is calculated by the NEURON simulation package (Hines and Carnevale, 1997). Cytoplasmic resistivity, specific membrane capacitance, and specific membrane resistance were set to 150 Ohm.cm, 0.75 μF/cm^2, and 100,000 Ohm*cm^2, respectively, with the reversal potential for the leak conductance set at −50 mV. Active conductances followed activation-inactivation Hodgkin–Huxley kinetics (Table 1).

Parameters for I_A, I_{CaL}, I_{KCa}, and I_H were based on previously published values for SNc DA neurons (Wilson and Callaway, 2000; Amendola et al., 2012; Engel and Seutin, 2015). Fast sodium and potassium currents were derived from Migliore and Schild models (Schild et al., 1993; Migliore et al., 2008), respectively. The SK current is solely activated by an increase in calcium concentration. Therefore, intracellular calcium uptake was modeled as a simple decaying model according to Destexhe et al. (1993). Conductance values were set according to our own measurements or published values (Table 1). Consistent with the literature (Zhou et al., 1998; Kole et al., 2008; Hu et al., 2009; Gonzalez-

Cabrera et al., 2017), g_{Na} and g_{KDR} densities are higher in the AIS than in the rest of the neuron so that AP always initiates in the AIS. According to Gentet and Williams (2007), I_A density and inactivation kinetics were higher and depolarized, respectively, in the soma compared with the dendritic arbor. Initializing potential was set at −70 mV, and analysis was performed after pacemaking frequency reached a steady state (8 spikes). Each simulation run had a 6000 ms duration with a dt of 0.01 ms. All dendritic compartments and the axon-start compartment contained all currents, whereas AIS and axon only contained fast sodium and potassium currents (g_{Na}, g_{KDR}). Unless otherwise stated, all currents but the fast sodium and potassium currents had fixed and homogeneous conductance values in the dendrites and the axon-start compartment.

For the realistic morphology models, exact dendrite lengths, soma volume, diameters of primary dendrites, ABD secondary dendrites, axon, and AIS were used (for details, see Moubarak et al., 2019). The specific branching patterns of each neuron (topology) were also respected. In order to be consistent with the NEURON software constraints, soma volume was implemented by computing the equivalent cylinder corresponding to the volume measured using "fill out path" method on Simple Neurite Tracer. Axonal diameter was considered constant and set to the diameter of the distal part of the AIS, while the diameters of non-primary dendrites were approximated by a regular tapering to reach a final diameter of 0.5 µm.

Firing frequency and AP analysis (amplitude, first and second derivative of APs) were computed online by handmade routines directly written in NEURON hoc language. For the dendrotomy simulation, dendritic cut was modeled by decreasing the diameter of the cut branch to nearly zero (1 pm). All computing files are available at model DB database (entry #267306).

Experimental design and statistical analysis. Statistical analysis (performed according to data distribution) included the following: linear regression, multiple linear regression, unpaired *t* test, Mann–Whitney, and paired *t* test, with a *p* value <0.05 being considered statistically significant. Distribution of data was first tested for normality with the Shapiro–Wilk test. Then, the difference between means of two samples was accordingly computed using *t* tests or Wilcoxon signed rank tests. Linear regressions were obtained with the Pearson or Spearman test depending on normality of variable distribution. When needed, comparisons between correlations were made by bootstrapping ($n = 10{,}000$, bootcorci R package) (Rousselet et al., 2021). *p* values for regressions were corrected for multiple comparisons with a false discovery rate procedure (Benjamini and Hochberg, 1995). Multiple regressions were computed as a linear model, such as HW= a*ABD +b*ABD + error. Predictive values of the multiple linear models were tested by multiple repeated cross-validation (R caret package) (Kuhn, 2021). Briefly, data were randomly partitioned into train and test data (80%/20%). Repeated (20 times) 10-fold cross-validation was computed on train data, and the model was tested against the test data to calculate the *r*. This procedure was repeated 100 times to calculate the mean and CI (95%) for *r* and the model coefficients. Unless otherwise stated, statistical data are given as mean ± SD, and *n* indicates the number of recorded neurons. Statistical tests were computed by using Sigmaplot 11.0 software (Systat Software) and R (R Core Team, 2020).

Figure preparation. Figures were prepared using Sigma Plot, Prism 6, Adobe Photoshop, and Adobe Illustrator (CS5-CS6, Adobe Systems), and ImageJ (Schindelin et al., 2012; Schneider et al., 2012; Rueden et al., 2017), with brightness and contrast adjustments performed consistently across the images to enhance clarity.

Results

The dataset (neuronal reconstruction and associated electrophysiological recordings) used in the current study was already the object of a previous publication (Moubarak et al., 2019) where it was used to investigate the link between AIS morphology, SD sodium channels, and pacemaking. Additional morphological and electrophysiological analyses were performed for the current article. Moreover, dendrotomy experiments and new modeling simulations were specifically performed for the current study.

To explore the link between AP properties and morphology in SNc DA neurons, we performed somatic patch-clamp recordings combined with *post hoc* reconstructions of neuronal morphological based on neurobiotin fills of the recorded neurons ($n = 38$). AnkyrinG immunostaining was used to identify the axon (Meza et al., 2018; Moubarak et al., 2019), and the morphological properties of the ABD and nABDs were analyzed (Figs. 1, 2). In SNc DA neurons, the AP is initiated at the AIS and back-propagates sequentially through the ABD stem, the soma, and the nABDs (Hausser et al., 1995). This back-propagation relies on SD sodium channels (Hausser et al., 1995; Seutin and Engel, 2010; Moubarak et al., 2019), which also participate in the genesis of spontaneous pacemaking activity (Tucker et al., 2012; Jang et al., 2014; Moubarak et al., 2019). We therefore wondered whether the shape of the AP recorded at the soma could be influenced by the morphological properties of the dendritic arbor (Fig. 1).

We focused in particular on the overall length of the ABD and nABDs as well as the number of dendritic segments comprising them (Figs. 1*A*, 2). This analysis was performed on the 34 neurons where the axon arose from an ABD (34 of 38, 90%). The ABD was significantly longer (1008 ± 495 µm vs 532 ± 283 µm; $t = 5.07$, $p < 0.001$, $n = 34$, paired *t* test) and more complex (containing more dendritic segments; 12.1 ± 6.1 vs 5.2 ± 3.2; $t = 5.74$, $p < 0.001$, $n = 34$, paired *t* test) than any nABD (Fig. 2). On average, the starting diameter was also found to be significantly larger for the ABD than for the nABDs (3.7 ± 0.9 µm vs 2.8 ± 0.6 µm; $t = 5.77$, $p < 0.001$, $n = 34$, paired *t* test). Notwithstanding these differences in the average morphology of the ABD and nABDs, the relative contribution of the ABD and nABDs to the overall dendritic tree was extremely variable from neuron to neuron (Figs. 1*A*, 2). As previously described (Amendola et al., 2012; Dufour et al., 2014; Moubarak et al., 2019), the duration of the AP recorded at the soma also displayed considerable cell-to-cell variations, ranging from 0.9 to 1.81 ms (1.33 ± 0.20 ms, $n = 37$). Intriguingly, we found that AP HW was significantly correlated, albeit in opposite ways, with the complexity and the length of the ABD and nABDs (Fig. 1*B*,*C*). Specifically, the number of dendritic segments in the ABD and its length were negatively correlated with AP HW, while the same parameters for the nABDs were positively correlated with AP HW (Fig. 1*B*,*C*). The morphological properties of the ABD and nABDs were independent from each other (Fig. 2), and we combined them to perform multiple linear regressions against AP HW (Fig. 1*B*,*C*). Using ABD/nABD complexity or length, AP HW could be predicted with a Pearson correlation coefficient > 0.82. Multiple linear models obtained by cross-validation (see Materials and Methods) predicted a correlation with similar *r* values ($r = 0.75$, $CI_{95} = 0.63$-0.86). While AP HW is a "standard" parameter used to describe AP shape, it is merely a phenomenological measurement that captures the combined variations in rising and decaying rates of the AP (HW = 2.43 − 1.96*(rise slope) + 20.4*(decay slope); all terms significant $p < 0.001$, adjusted $r^2 = 0.8$, $p < 2 \times 10^{-16}$, $n = 37$, multiple linear regression), which are more closely related to the density of inward and outward currents underlying the AP (Bean, 2007). Consistent with this, both rising and decay rates were also significantly correlated with ABD complexity ($r = 0.41$, $p = 0.0011$ and $r = -0.54$, $p = 0.0005$, respectively). Thus, although ion channel properties and densities vary from cell to cell (Liss et al., 2001; Seutin and Engel, 2010; Amendola et al., 2012; Moubarak et al., 2019; Haddjeri-Hopkins et al., 2021)

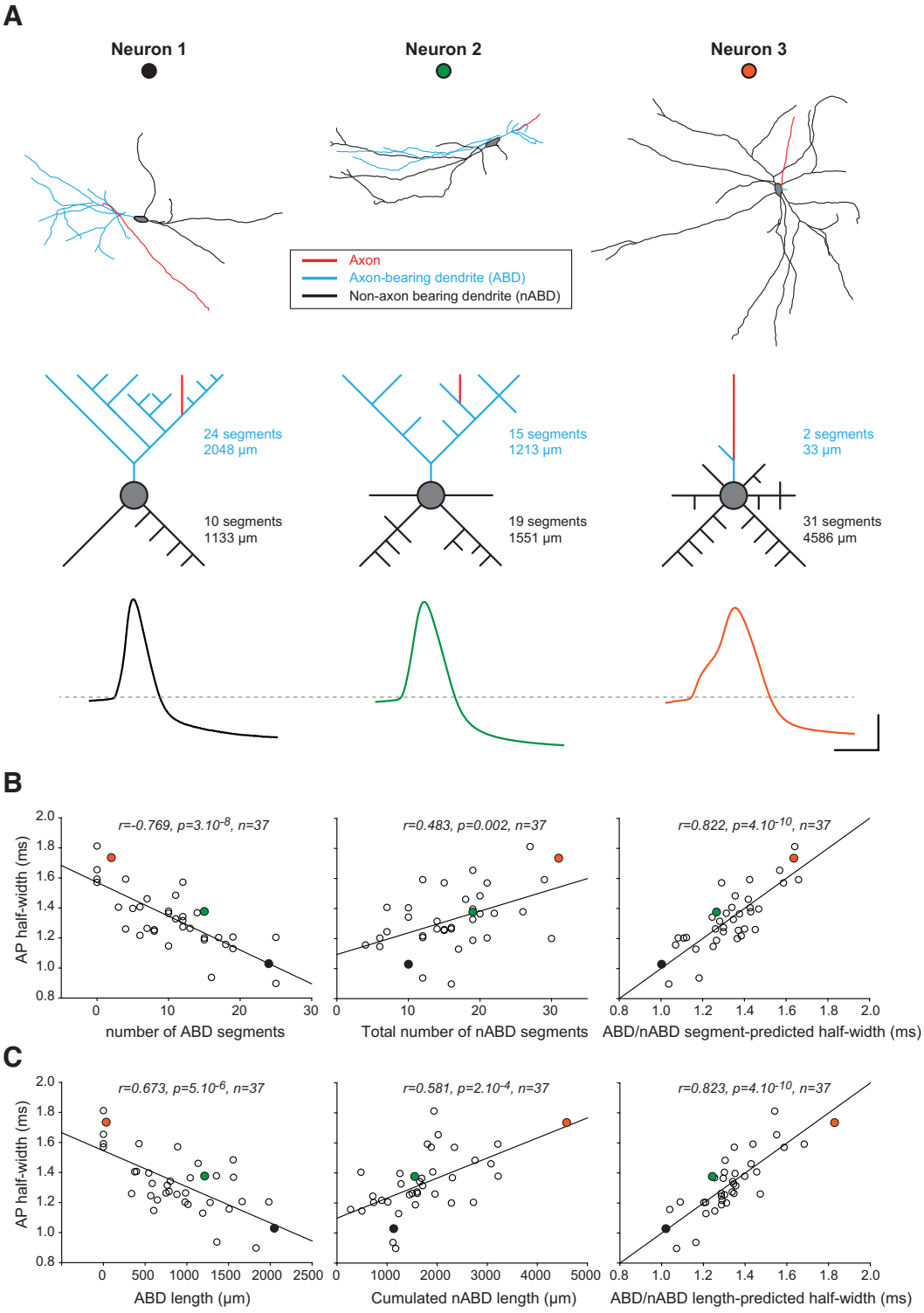

Figure 1. Dendritic topology predicts somatic AP half-width in SNc DA neurons. ***A***, Top row, Skeleton pictures of three fully reconstructed SNc DA neurons. Middle row, Schematic representations of the topology corresponding to the same three neurons. The number of dendritic segments comprising the ABD (blue) and the nABDs (black) as well as their respective lengths are indicated. Bottom row, Somatic current-clamp recordings of the AP obtained in the same three neurons. The AP is getting slower when the complexities of the ABD and nABDs are decreasing and increasing, respectively. ***B***, Left, Scatter plot representing the negative correlation between ABD complexity and AP half-width. Middle, Scatter plot representing the positive correlation between nABD complexity and AP half-width. Right, Scatter plot representing the correlation obtained using a linear combination of ABD and nABD complexities (multiple linear correlation). ***C***, Left, Scatter plot representing the negative correlation between ABD length and AP half-width. Middle, Scatter plot representing the positive correlation between nABD length and AP half-width. Right, Scatter plot representing the correlation obtained using a linear combination of ABD and nABD lengths (multiple linear correlation). Black, green, and orange dots represent specific values obtained for the three neurons presented in ***A***. Calibration: ***A***, vertical 20 mV, horizontal 2 ms. Horizontal dotted line indicates AP threshold.

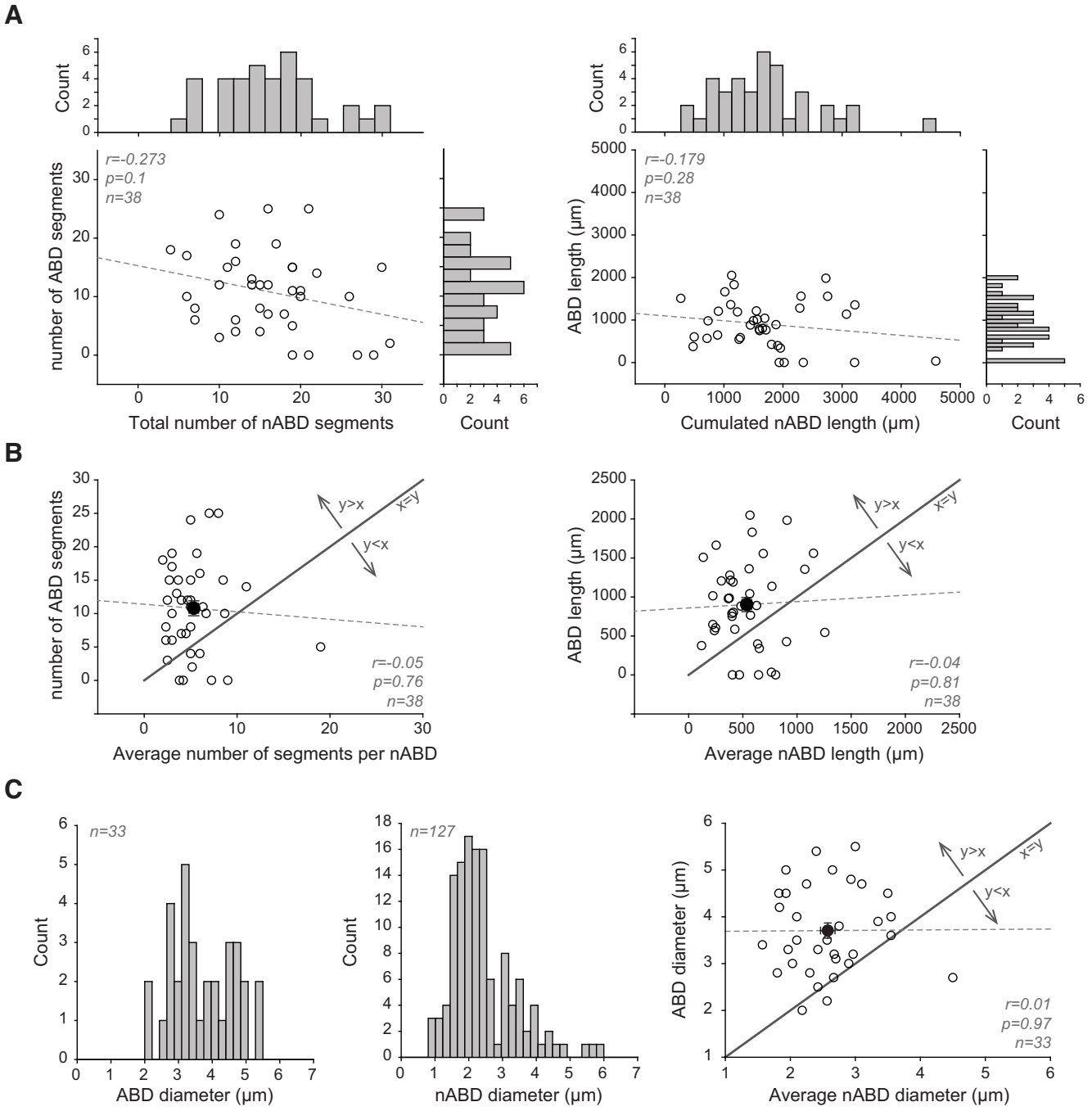

Figure 2. Detailed description and comparison of ABD and nABD morphological properties. ***A***, Left, Scatter plot representing the lack of relationship between the total complexity of the nABDs and the complexity of the ABD. Histograms represent the distribution of values for the number of segments of the ABD and nABDs, displayed on the right and top of the scatter plot, respectively. Right, Scatter plot representing the lack of relationship between the cumulated length of the nABDs and the length of the ABD. Histograms represent the distribution of values for the length of the ABD, and nABDs are displayed on the right and top of the scatter plot, respectively. ***B***, Left, Scatter plot representing the complexity of the ABD versus the average complexity of a nABD. Black dot represents the average measured in 38 neurons. Plain line indicates the identity line. The number of segments per nABD is not correlated with the number of segments per ABD, and the number of segments per ABD is on average larger than the number of segments per nABD. Right, Scatter plot representing the length of the ABD versus the average length of a nABD. Black dot represents the average measured in 38 neurons. Plain line indicates the identity line. The average length of a nABD is not correlated with the length of the ABD, and the length of the ABD is on average larger than the average length of a nABD. ***C***, Left and middle, Histograms representing the distribution of values for the diameters of the ABD and the nABDs measured in 33 and 37 neurons, respectively. Right, Scatter plot representing the diameter of the ABD versus the average diameter of a nABD. The average diameter of a nABD is not correlated with the diameter of the ABD, and the diameter of the ABD is on average larger than the average diameter of a nABD.

and have been shown to control AP back-propagation (Moubarak et al., 2019), knowing the specific dendritic topology of an SNc DA neuron (complexity of the ABD and nABDs) is sufficient to predict 68% (r^2) of the variance in duration of the AP at the soma, suggesting that dendritic topology largely constrains AP duration. None of the other parameters defining AP shape (amplitude, threshold, AfterHyperPolarization voltage) shared a significant correlation with morphological measurements.

In order to investigate the potential biophysical underpinnings of this unexpected relationship, we then used a multicompartment Hodgkin–Huxley model based on the precise morphological measurements obtained from the 37 neurons where electrophysiological

recordings were performed (for details, see Moubarak et al., 2019). The opposite correlations shared by the ABD or nABDs with AP HW suggest contrasting influences of these dendritic branches on AP shape. While the ABD can be viewed as an accelerator of the AP (complexity/length negatively correlated with AP HW), the nABDs seem to slow down the AP (complexity/length positively correlated with AP HW). Another way of seeing it is that the ABD has an "active" influence on the shape of the somatic AP while the nABDs mainly act as a "passive sink" (Brette, 2013; Kole and Brette, 2018). The sodium and L-type calcium channels are the main depolarizing conductances defining the upstroke of the AP in SNc DA neurons (Bean, 2007; Puopolo et al., 2007; Seutin and Engel, 2010; Philippart et al., 2016), suggesting that their density in the ABD may be critical for AP HW. We therefore tested whether the opposite correlations between ABD or nABDs and AP HW could be explained solely by an increase in ABD complexity or whether a different density of inward conductances in the ABD was also needed. The average density of sodium conductance (g_{Na}) in the dendrites of rat SNc DA neurons, measured in a previous study (Moubarak et al., 2019), has been estimated to be ~75 pS/μm^2, while the dendritic density of L-type calcium current (g_{Ca}) is unknown. We linearly and independently increased g_{Na} and g_{Ca} in the ABD up to ~3-fold while keeping their density constant in the soma and nABDs, starting with a baseline g_{Na} of either 75 or 50 pS/μm^2 and a baseline g_{Ca} of 1 pS/μm^2 (Figs. 3, 4). Using this approach, a database of 231 models for each of the 37 reconstructed neurons was created (Fig. 4*A*). In all conditions, these models of SNc DA neurons still generated a pacemaking pattern of activity in the expected range of frequencies (Fig. 3*B*). We then analyzed whether the correlations between ABD or nABD complexity and AP HW observed in the real neurons were reproduced in the model and how they were influenced by increasing g_{Na}, g_{Ca}, or both, in the ABD compared with the nABDs (Figs. 3*C*, 4*A*). While the positive correlation between nABD complexity and AP HW was fairly insensitive to changes in ABD g_{Na} and g_{Ca}, the negative correlation between ABD complexity and AP HW was present only when ABD g_{Na} (and/or g_{Ca}) was increased (Fig. 3*C*). Indeed, simultaneously increasing both conductances very much improved the power of this correlation, such that the multiple linear regression based on ABD and nABD complexities was significant only in this case (Figs. 3*C*, 4*A*), with a Pearson correlation factor close to the one observed in real neurons ($r = 0.76$, $p = 7 \times 10^{-8}$, $n = 36$ in the model compared with $r = 0.82$, $p = 4 \times 10^{-10}$, $n = 37$ in the real neurons). Multiple linear models obtained by cross-validation (see Materials and Methods) predicted a correlation with similar r values ($r = 0.60$, CI_{95} = 0.52-0.70). Consistent with the experimental results reported before (Fig. 1*C*), similar results were obtained when using the length of the ABD and nABDs instead of their complexity (data not shown). Most interestingly, in the heterogeneous condition (g_{Na}/g_{Ca} increased in the ABD), the half-width of the AP produced by the model neurons predicted the half-width of the AP recorded in the real neurons ($r = 0.72$, $p = 1 \times 10^{-6}$, $n = 35$, Fig. 3*C*). Since other conductances are involved in defining AP duration (e.g., the delayed rectifier potassium current) or have been suggested to display a higher conductance density in the ABD (e.g., I_H) (see Engel and Seutin, 2015), we tested whether increasing ABD excitability by the manipulation of these conductances (decreasing g_K or increasing g_H in the ABD) had a similar effect on the observed correlations. While the positive correlation between nABD complexity and AP HW was present in all conditions, the negative correlation between ABD complexity and AP HW was not reproduced in models where g_H or g_K was increased or decreased, respectively, in the ABD (Fig. 4*B*,*C*). Thus, the correlation between dendritic topology and AP duration observed in real neurons can only be reproduced in a realistic model if g_{Na} and g_{Ca} specifically are larger (by ~2-fold) in the ABD compared with the nABDs. Moreover, this condition of heterogeneous dendritic excitability allows the model to predict the duration of the somatic AP recorded in the real neurons. Since modifications in dendritic biophysical properties (increased g_{Na}/g_{Ca}) were identical for all model neurons, cell-to-cell variations in dendritic topology are sufficient to explain most of the variation in somatic AP shape observed in real neurons.

So far, the relationships between dendritic topology and AP duration observed in the real neurons and their realistic computer-simulated counterparts are only correlative. However, since our model is purely deterministic, these correlations suggest that increasing the complexity/length of the ABD indeed "speeds up" the AP while increasing the complexity/length of the nABDs "slows it down." We therefore tested the causality of the variables by simulating ABD and nABD dendrotomies and determined how g_{Na}/g_{Ca} conductance distribution influenced the effect of these manipulations (Fig. 5). ABD and nABD dendrotomies were simulated on the same neurons using both the homogeneous (same g_{Na}/g_{Ca} in ABD and nABDs, model 1) and heterogeneous (increased g_{Na}/g_{Ca} in the ABD, model 4) versions of the model. On the ABD side, dendrotomies of intermediate dendrites (located in between the axon and the soma) or distal dendrites (more distal from the soma than the axon) were tested (Fig. 5*A*): these two manipulations produced similar effects on AP HW and were thus pooled in our statistical analysis. Simulating a dendrotomy of the ABD or nABDs in the homogeneous model had the same effect on AP HW, inducing a small but significant decrease in AP HW (ABD, 100% vs 98.14%, $t = 6.88$, $p < 0.001$, $n = 44$, paired t test; nABD, 100% vs 96.26%, $z = -5.16$, $p < 0.001$, $n = 37$, signed rank test; Fig. 5*B*, *C*). However, in the heterogeneous version of the model, ABD and nABD dendrotomies had opposite effects on AP HW: sectioning the nABD still induced a decrease in AP HW (100% vs 94.92%, $z = -5.16$, $p < 0.001$, $n = 35$, signed rank test; Fig. 5*B*, *C*), while sectioning the ABD significantly increased AP HW (100% vs 102.55%, $t = 6.62$, $p < 0.001$, $n = 41$, paired t test; Fig. 5*C*). Thus, an increased g_{Na}/g_{Ca} in the ABD confers opposite causal influences to the ABD and nABDs on AP duration, hence corroborating the opposite correlations observed between ABD or nABDs and AP HW in real neurons and in the models (Figs. 1, 3).

Based on this prediction from the model, we sought to determine whether experimentally reducing dendritic complexity by specific ABD and nABD dendrotomies would have opposite effects on AP HW in real neurons (Fig. 6). In order to test this hypothesis, neurons were filled with Alexa-594 during patch-clamp recording, and laser illumination (line scan) was used to induce dendrite photo-ablation (Fig. 6*A*,*B*). The nature of the sectioned dendrite (ABD vs nABD) was determined by *post hoc* neurobiotin and ankyrinG immunohistochemistry, which allowed us to define the location of the axon (Fig. 6*A*). APs were triggered by injecting incremental current steps, and the relationship between AP amplitude and AP HW was defined for each neuron before and after photo-ablation (Fig. 6*C*). AP amplitude and AP HW were negatively correlated, and the slope of this relationship was modified by dendrite photo-ablation. Although the range of AP amplitudes was usually modified after photo-ablation, we could calculate the change in AP HW for APs of the same amplitude before

A

	nABD		soma		ABD	
	g_{Na}	g_{Ca}	g_{Na}	g_{Ca}	g_{Na}	g_{Ca}
Model #1 (homogeneous)	75	1	75	1	75	1
Model #2 (heterogeneous g_{Ca})	75	1	75	1	75	**2.2**
Model #3 (heterogeneous g_{Na})	**50**	1	**50**	1	**120**	1
Model #4 (heterogeneous g_{Na}/g_{Ca})	**50**	1	**50**	1	**120**	**2.2**

B

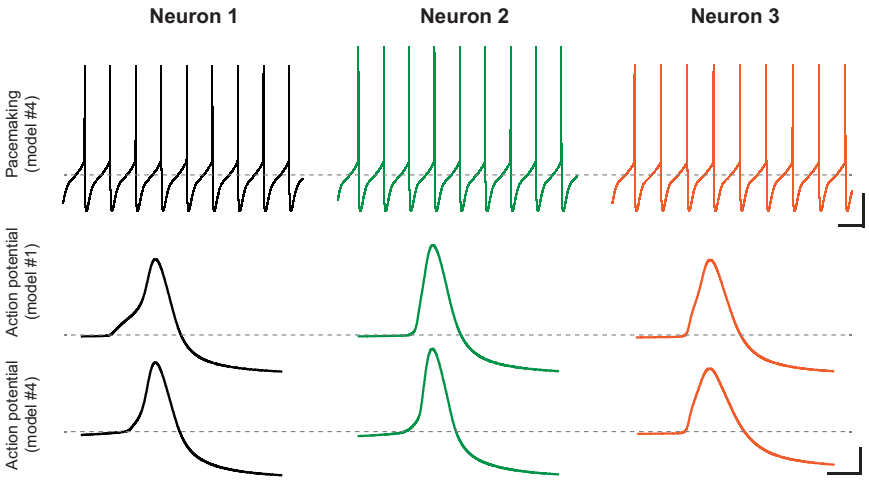

C

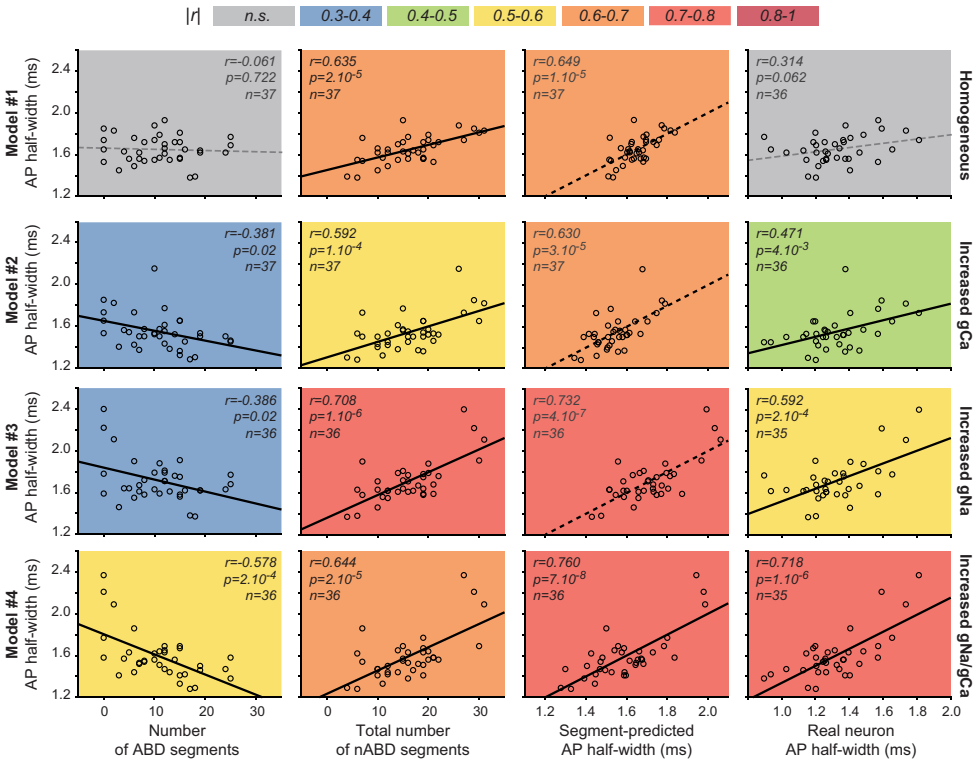

Figure 3. A realistic morphology model of SNc DA neurons reproduces the correlations between dendritic topology and AP half-width and predicts the recorded AP half-width. ***A***, Table representing the specific values of sodium (g_{Na}) and calcium conductance (g_{Ca}) implemented in the nABDs, soma, and ABD in the four versions of the model presented in the rest of the figure. ***B***, Top row, Example traces representing the voltage waveforms of spontaneous activity produced by the model 4 for the models of the three neurons presented in Figure 1. Middle and bottom rows, AP waveforms obtained for the same neurons for the models #1 and #4, respectively. ***C***, Scatter plots representing the relationships between ABD complexity (first left), nABD complexity (second left), a linear combination of ABD and nABD complexity (second right), or the AP half-width measured in real neurons (first right) and the AP half-width measured in the realistic morphology models. The relationships are shown for the four versions of the model (top to bottom) presented in ***A***. Gray dotted lines indicate nonsignificant correlations. Scatter plots are color-coded, depending on the value of the correlation coefficient. Dotted lines for the multiple linear correlations indicate that only one variable (nABD complexity) significantly participates in the

and after dendrotomy (Fig. 6*C–E*). Because of the severity of the experimental manipulation, this experiment could only be conducted on 7 neurons, including 3 nABD dendrotomies, 2 ABD dendrotomies, and 2 control neurons where laser illumination failed to induce dendrite photo-ablation. Consistent with the correlations described in Figure 1 and the model predictions, nABD dendrotomy was associated with a decrease in AP HW (100% vs 89.4%, $n = 3$), ABD dendrotomy was associated with an increase in AP HW (100% vs 113.65%, $n = 2$), while the absence of photo-ablation was associated with no change in AP HW (100% vs 99.1%, $n = 2$; Fig. 6*D*). These experiments strongly suggest that the opposite correlations between the topology of the ABD or nABDs and AP HW described in Figure 1 arise because the ABD and nABDs have opposite causal influences on AP HW. Based on the modeling results (Fig. 5), they also reinforce the hypothesis that sodium channel density must be higher in the ABD than in nABDs. As sodium channels are supposed to mainly define the rising phase of the AP, we wondered whether AP HW modifications following dendrotomy were always because of changes in AP rise slope (Fig. 6*E*). Interestingly, as can be seen on the traces (Fig. 6*C*), both the rise and decay phases were modified after dendrotomy, although ABD and nABD dendrotomies appeared to affect AP dynamics differently: the AP HW increases (ABD cut) were associated with a slowing down of AP decay, while the AP HW decreases (nABD cut) were mainly because of an acceleration of AP rise (Fig. 6*E*).

We then pursued the investigation of the biophysical mechanisms underlying the cell-to-cell variations in AP HW by precisely quantifying the variations in AP amplitude and decomposing the AP rising phase in initial segment (IS) and SD components using the voltage first derivative (Fig. 7*A*) (Moubarak et al., 2019). We then determined whether the variations in these properties were correlated with variations in AP HW, rise and decay slopes in real neurons, and whether these relationships were reproduced in our model (Fig. 7*B*,*C*). As the heterogeneous model better reproduced the experimental results, we will only present the results from this version, although both versions were tested and analyzed. AP HW was not correlated with AP amplitude across recorded neurons, and rise slope appeared essentially defined by the SD component and independent of the variation in IS component amplitude (Fig. 7*B*). Analyzing the correlations between AP HW and rise and decay slopes in real neurons then revealed that AP HW is mainly determined by the decay rate of the AP ($r = 0.97$ vs $r = -0.57$ for max rise, bootstrap Pearson comparison $p < 10^{-10}$), and that rise and decay slopes are significantly correlated with each other (Fig. 7*C*). These correlations between AP HW and rise or decay slopes were reproduced in the heterogeneous model (Fig. 7*C*). These results show that the shape of the somatically recorded AP is mainly determined by the SD sodium channels, and that its duration is defined mainly by its decay rate, although rise and decay rates are correlated such that they cannot be fully dissociated in their contribution to cell-to-cell variations in AP HW.

We then used our model to investigate which biophysical parameters are responsible for the variations in AP HW, rise slope, and decay slope (Fig. 8). In order to do so, we measured the AP properties (amplitude, HW, maximum rise slope, maximum decay slope) based on the voltage and first derivative signals, and also measured the main conductances active during the AP (Fig. 8*A*). Five conductances were initially considered: the fast sodium conductance (g_{Na}), the L-type calcium conductance (g_{Ca}), and the delayed rectifier (g_{KDR}), A-type (g_A), and calcium-activated (g_{KCa}) potassium conductances. However, g_{Ca} and g_{Kca} were rapidly discarded because they contribute very little to the overall conductance (and thus to voltage changes) during the AP. In addition, the calcium-activated potassium conductance (g_{Kca}) used in our model corresponds to an SK channel model (Destexhe et al., 1993) and is rather slow to contribute significantly to AP dynamics. While g_A had a very large peak conductance during the AP (mean = 15.21 μS/cm^2 compared with 10.56 for g_{Na} and 3.44 for g_{KDR}), its value was not correlated with the variations in AP HW, rise, and decay in both versions of the model (data not shown), suggesting that it does not play a major role in the control of AP duration. We thus focused on the profile of g_{Na} and g_{KDR} during the AP, extracting the peak conductances reached during the AP and the kinetics of activation (rise time, decay time, maximum rise slope, maximum decay slope) for both conductances. As can be seen on the traces in Figure 8*A*, variations in AP HW were associated with non-negligible changes in both amplitude and kinetics of g_{Na} in particular. As shown by the linear regression analysis (Fig. 8*B*), variations in g_{Na} and g_{KDR} peak conductances predicted the changes in AP amplitude, HW, rise, and decay slopes. In general, g_{Na} was a better predictor of AP variations than g_{KDR}, as revealed by the bootstrap analysis (significant differences for AP amplitude, $p < 10^{-10}$; AP max rise, $p < 0.01$; and AP max decay, $p < 0.05$). As already suggested by the traces shown in Figure 8*A*, variations in peak conductance were associated with changes in kinetics of g_{Na} and g_{KDR}: for each conductance, all kinetic parameters were correlated with peak conductance with r values >0.9 (larger conductances were faster), except for g_{KDR} rise time that was not significantly correlated with g_{KDR} peak conductance. On the other hand, g_{KDR} rise time was strongly correlated with g_{Na} peak conductance, rise, and decay slopes ($r > 0.89$). As AP decay slope appeared critical in defining AP HW (see Fig. 7), we tested the ability of conductance kinetics to predict it in both versions of the model (Fig. 8*C*). The two factors showing the best correlation with AP maximum decay slope were g_{Na} max decay slope and g_{KDR} max rise slope. Thus, the variations in kinetics of g_{Na} and g_{KDR} associated with changes in peak conductance are responsible for the observed variations in AP kinetics. Since our dendrotomy experiments suggested that changes in AP HW were because of changes in both AP rise and decay slopes (Fig. 6*E*), we then analyzed the changes in AP properties and in g_{Na} and g_{KDR} conductances in the dendrotomy simulations (Fig. 8*D*). Unlike in the experimental data, changes in AP rise and decay were similar (albeit of opposite signs) for ABD and nABD dendrotomies, such that all data could be pooled together ($n = 83$). Consistent with the results presented so far, changes in AP HW were correlated with changes in AP maximum rise and maximum decay slopes, although the correlation with decay was significantly better ($r = -0.89$, $p = 7 \times 10^{-29}$, $n = 83$ vs $r = -0.74$, $p = 8 \times 10^{-16}$, $n = 83$, bootstrap Pearson comparison, $p = 0.0048$). From a biophysical perspective, changes in AP maximum decay were best predicted by changes in g_{Na} decay kinetics (decay time) and g_{KDR} rise kinetics (rise time) (Fig. 8*D*), consistent with what we found in the cell-to-cell variation analysis (Fig. 8*C*). Thus, variations in AP half-width

←

correlation. Calibration: ***B***, top traces, vertical 20 mV, horizontal 200 ms; middle and bottom traces, vertical 20 mV, horizontal 2 ms. Horizontal gray dotted lines indicate −60 mV (top traces) and AP threshold (middle and bottom traces).

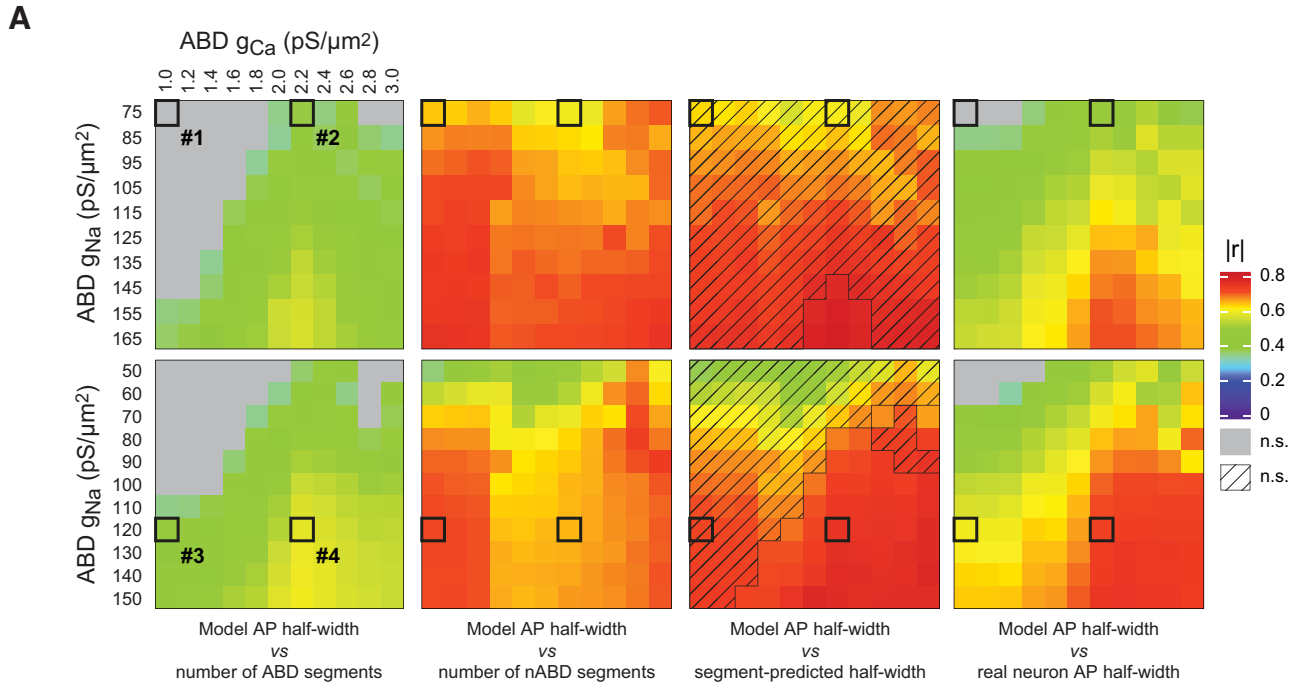

B

	nABD		soma		ABD	
	g_H	g_K	g_H	g_K	g_H	g_K
Model #1 (homogeneous)	0.5	150	0.5	150	0.5	150
Model #5 (heterogeneous g_H)	0.5	150	0.5	150	**2**	150
Model #6 (heterogeneous g_K)	0.5	150	0.5	150	0.5	**50**

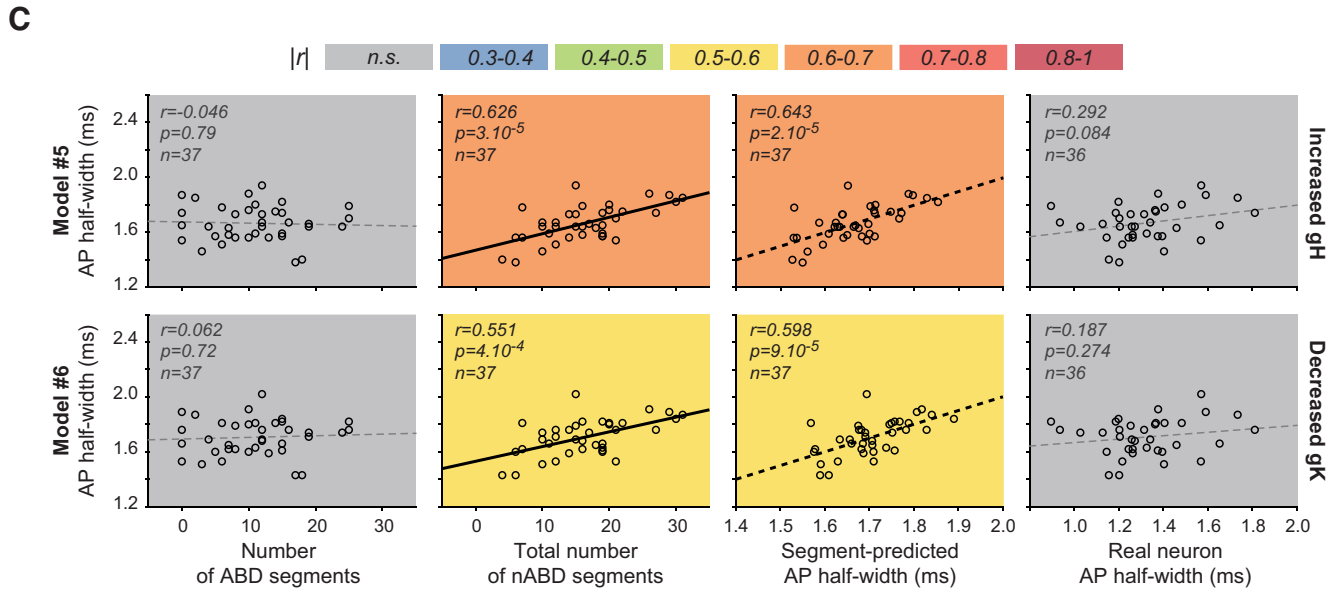

Figure 4. Exploring the biophysical conditions necessary to reproduce the correlation between dendritic topology and AP half-width. ***A***, Heatmaps representing the evolution of the correlation factor *r* for the relationships presented in Figure 2*C* when independently and linearly varying g_{Ca} in the ABD from 1 to 3 pS/µm^2 (top and bottom heatmaps) and g_{Na} in the ABD from 75 to 165 pS/µm^2 (top) or from 50 to 150 pS/µm^2 (bottom). nABD conductance values were kept fixed at 1 and 75 pS/µm^2 (top) or 1 and 50 pS/µm^2 (bottom) for g_{Ca} and g_{Na}, respectively. The four versions of the model presented in Figure 2 are highlighted by a dark surrounding. Shaded area in the heatmap represents the multiple linear regression (second right), indicating that only one variable (nABD complexity) significantly participates in the correlation. ***B***, Table representing the specific values of I_H (g_H) and delayed rectifier potassium conductance (g_K) implemented in

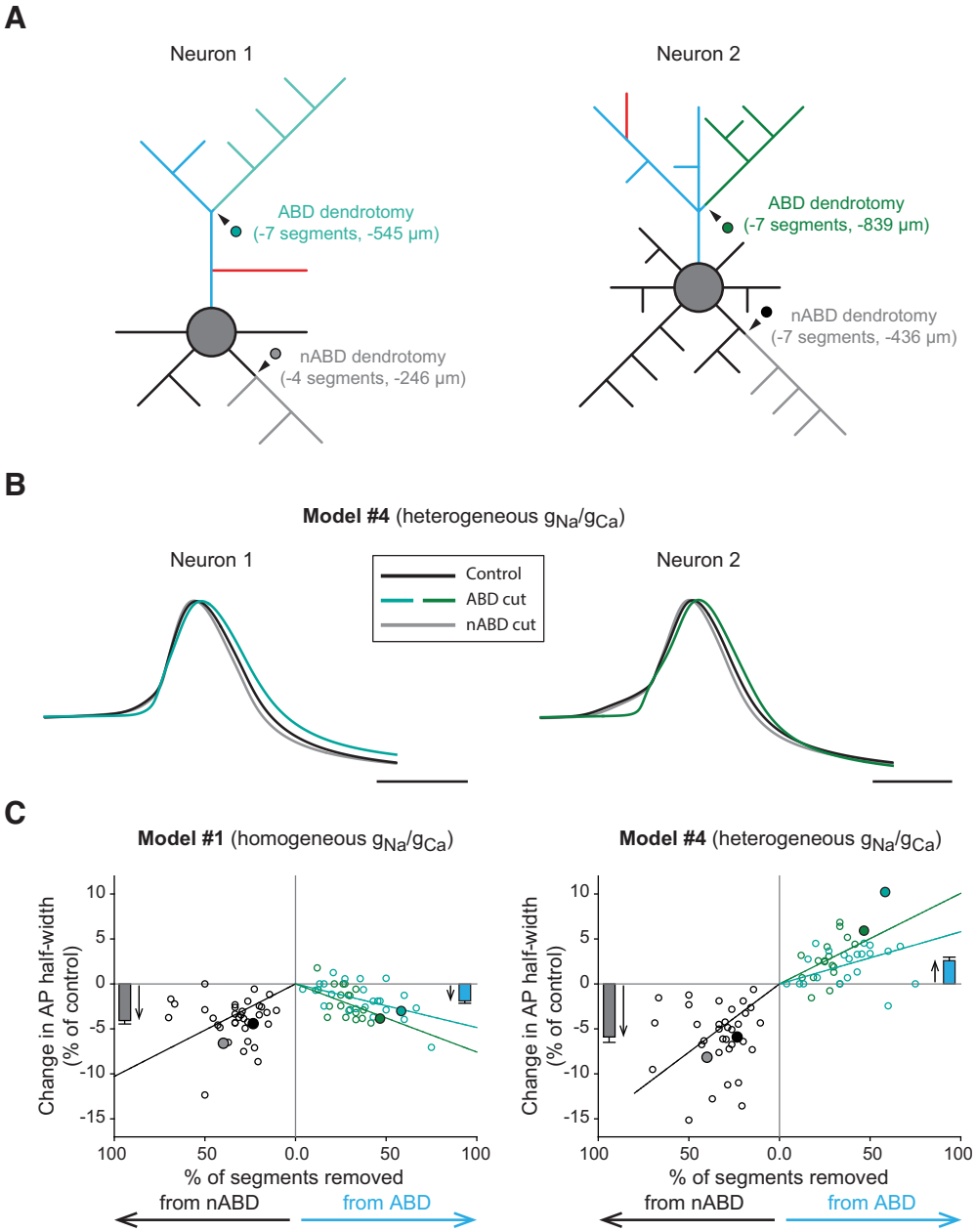

Figure 5. Modeling the effect of ABD and nABD dendrotomies. ***A***, Schematic representations of the topology of two neurons, indicating the location and extent of the dendrotomies simulated on the ABD (green dots) or nABD (gray and dark dots). ***B***, Voltage waveforms of the AP obtained for the model 4 of neuron 1 (left) and neuron 2 (right) before dendrotomy (black trace), and after ABD (green) or nABD dendrotomy (gray). AP waveforms were scaled and aligned at mid-amplitude to allow comparison of the half-widths. ***C***, Scatter plots representing the change in AP half-width following simulated dendrotomy in the model 1 (left) and 4 (right) as a function of the percentage of nABD or ABD segments removed from the model. The average changes in AP half-width obtained for nABD and ABD dendrotomies are indicated as bar plots (mean ± SEM) on each scatter on the left and right, respectively. Only the model 4 predicts an opposite influence of nABDs and ABD on AP half-width. Scale bars: ***B***, 2 ms.

←

the nABDs, soma, and ABD in the two versions of the model presented in ***C***. ***C***, Scatter plots representing the relationships between ABD complexity (first left), nABD complexity (second left), a linear combination of ABD and nABD complexity (second right), or the AP half-width measured in real neurons (first right) and the AP half-width measured in the realistic morphology models. The relationships are shown for the two versions of the model (#5, top; #6, bottom) presented in ***B***. Gray dotted lines indicate nonsignificant correlations. Scatter plots are color-coded, depending on the value of the correlation coefficient. Dotted lines for the multiple linear correlations indicate that only one variable (nABD complexity) significantly participates in the correlation.

seem to be mainly because of changes in AP decay rate, which is itself explained by variations in g_{Na} decay and g_{KDR} rise kinetics.

Discussion

In this study, we demonstrated that somatic AP shape in SNc DA neurons is strongly constrained by the specific topology of the dendritic arborization because of the opposite influence of the ABD and nABDs on AP duration. Using computational modeling, we showed that this influence of dendritic topology on AP shape requires a slightly higher density of sodium and calcium channels in the ABD. Moreover, our results suggest that

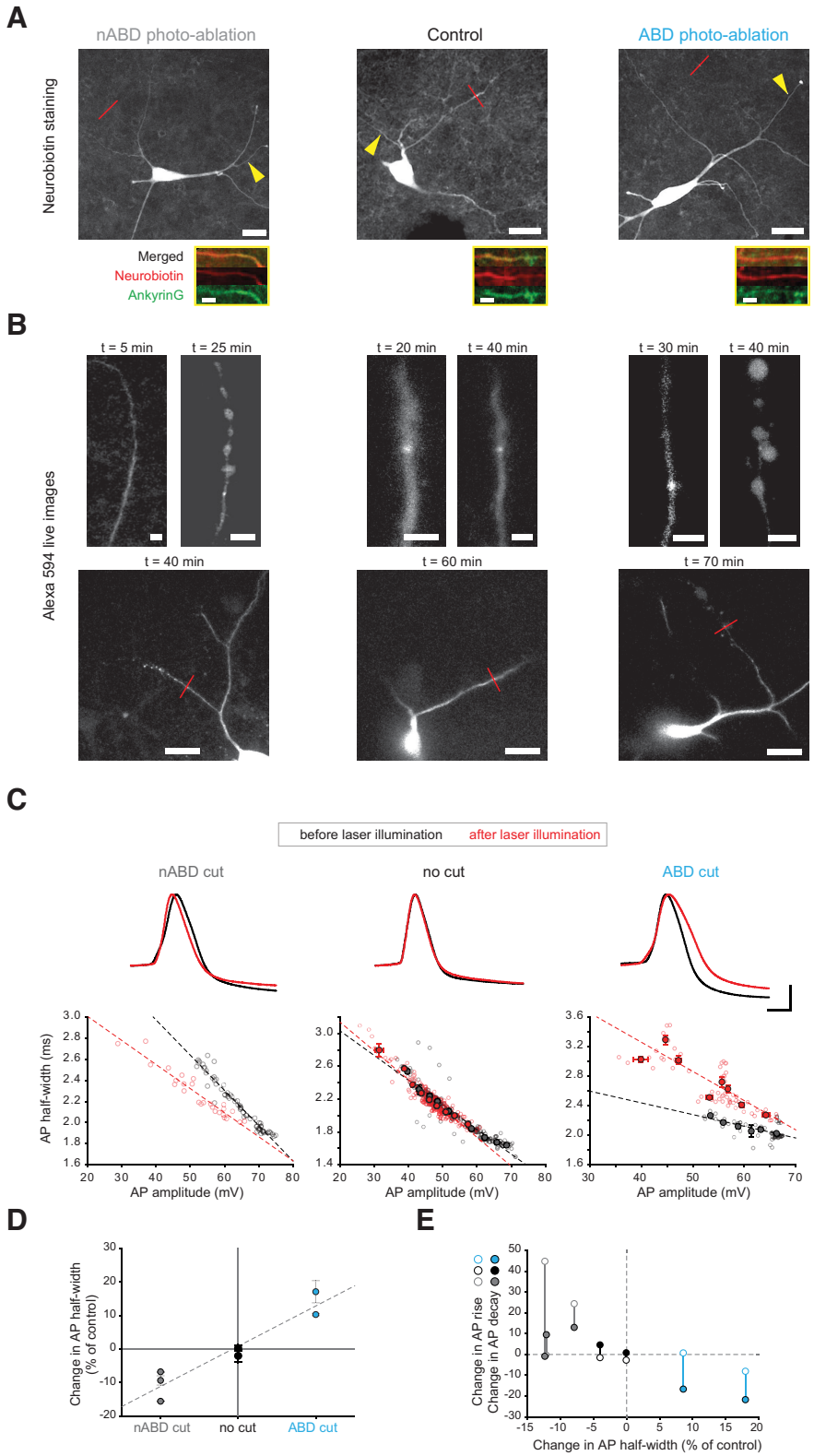

Figure 6. Dendrite photo-ablation confirms the opposite influence of nABDs and ABDs on AP half-width. ***A***, Top, Confocal images of *post hoc* neurobiotin immunostaining of three neurons on which a dendritic photo-ablation experiment was performed (left, nABD dendrotomy; middle, no dendrotomy after laser illumination; right, ABD dendrotomy). Red line indicates where laser illumination (line scan) was performed. Yellow arrowhead indicates the axon (identified by *post hoc* ankyrinG immunostaining). Bottom, Zoomed-in confocal images representing the superposition (merged image) of the neurobiotin (red) and ankyrinG stainings (green) used for the identification of the AIS. ***B***, Top, Zoomed-in confocal live images representing the dendritic branch before laser illumination and after effective laser illumination for the three neurons presented in the top row images. Bottom, Zoomed-out confocal live images representing neuronal morphology after laser illumination. Red line indicates the exact location of laser illumination. ***C***, Top, AP waveforms recorded in the three neurons presented in ***A*** before (black traces) and after laser illumination (red traces). APs displaying a similar amplitude were chosen to allow comparison of the half-widths. Bottom, Scatter plots representing the relationship between AP amplitude and AP half-width before (black dots) and after laser illumination (red dots) in the same neurons presented in ***A*** and ***B***. Light colors represent individual APs. Binned and averaged values (with error bars, SEM) appear in dark color when the number of APs allowed averaging. Dotted lines indicate the linear regression depicting the relationship between AP amplitude and half-width. ***D***, Scatter plot representing the effect of dendrotomy on AP half-width observed in 8 neurons (3 nABD cut, gray dots; 3 controls, black dots; 2 ABD cut, blue dots). ***E***, Scatter plot representing the changes in AP rise slope (open circles) and in AP decay slope (closed circles) associated with the changes in AP half-width. The color coding used here is the same as in ***D***. Scale bars: ***A***, top 25 µm, bottom 5 µm; ***B***, top 5 µm, bottom 25 µm. Calibration: ***C***, vertical 20 mV, horizontal 2 ms.

these morphology-related variations in AP shape are mainly because of changes in AP decay rate, which are themselves essentially determined by the effective SD sodium conductance activated during the AP, its kinetics, and its effect on the activation of the delayed rectifier conductance.

The most important finding of our study is that the variation in dendritic topology in SNc DA neurons explains most of the cell-to-cell variation in half-width of the somatic APs (68% based on the multiple linear regressions presented in Fig. 1). To our knowledge, this is the first experimental study demonstrating that dendritic morphology can have a predominant influence on AP shape across neurons of the same type, such that AP duration can be reasonably well predicted on the sole basis of dendritic topology. Several studies have demonstrated that the biophysical properties of dendritic ion channels, including sodium channels, display substantial cell-to-cell variability in SNc DA neurons (Liss et al., 2001; Gentet and Williams, 2007; Seutin and Engel, 2010; Amendola et al., 2012; Engel and Seutin, 2015; Philippart et al., 2016; Moubarak et al., 2019). One may thus wonder whether their neuronal output is predominantly defined by variations in ion channel density or in dendritic morphology. A previous study dedicated to the role of dendritic sodium channels in pacemaking showed that cell-to-cell variations in dendritic morphology have a greater influence on the spontaneous firing rate than variations in sodium channel density (Moubarak et al., 2019). The current study goes one step further by demonstrating that variations in dendritic morphology

predict AP duration despite the substantial cell-to-cell variations in sodium channel density observed in this cell type. By showing that the relationship between dendritic topology and AP duration is reproduced when all neurons are endowed with identical sodium conductance density profiles, the computational modeling results reinforce these conclusions. Even so, we need to bear in mind that, at constant sodium conductance density, increasing dendritic complexity (and length) in the model leads to an increase in the overall sodium dendritic conductance. In these conditions, separating the influence of active and passive properties is particularly difficult. Moreover, although the precise dendritic lengths were included in the model, only the diameters of primary and secondary dendrites could be measured and implemented. Thus, model morphologies are not high-resolution replicates of the original morphology of the reconstructed neurons. Nonetheless, the goal of this study was rather to determine the minimal conditions required to explain the correlation observed between dendritic topology and AP duration. In this context, the most surprising result was that these conditions also enable the model to predict the duration of the AP recorded in real neurons, unambiguously demonstrating the predominant role of cell-to-cell variations in dendritic morphology in defining AP shape in this neuronal type.

So far, most studies investigating the sources of variations in AP properties (duration, amplitude, energy efficiency) were focused on the contribution of the biophysical properties of sodium and potassium currents to these processes (Alle et al., 2009, 2011; Carter and Bean, 2009, 2011; Sengupta et al., 2010). Moreover, these studies aimed at understanding the biophysical bases of differences in AP shape across neuronal types and not within the same neuronal population. Briefly, large variations in AP duration across neuronal types seem to be essentially determined by the types of potassium channels expressed (Rudy and McBain, 2001; Bean, 2007; Carter and Bean, 2009). In particular, the expression of Kv3 and/or BKCa channels appears necessary to achieve fast AP repolarization and fast-spiking patterns of activity (Rudy and McBain, 2001; Lien and Jonas, 2003; Alle et al., 2011; Kaczmarek and Zhang, 2017; Hunsberger and Mynlieff, 2020). On the other hand, the variations in properties of sodium channels do not seem to contribute significantly to the differences in AP duration observed across cell types (Carter and Bean, 2009). Consistent with this, studies investigating the maturation of AP shape demonstrated that changes in duration during postnatal development in a given neuronal type are mainly related to changes in potassium channel expression patterns (Hunsberger and Mynlieff, 2020; Sanchez-Aguilera et al., 2020), although changes in sodium current have also been observed in some

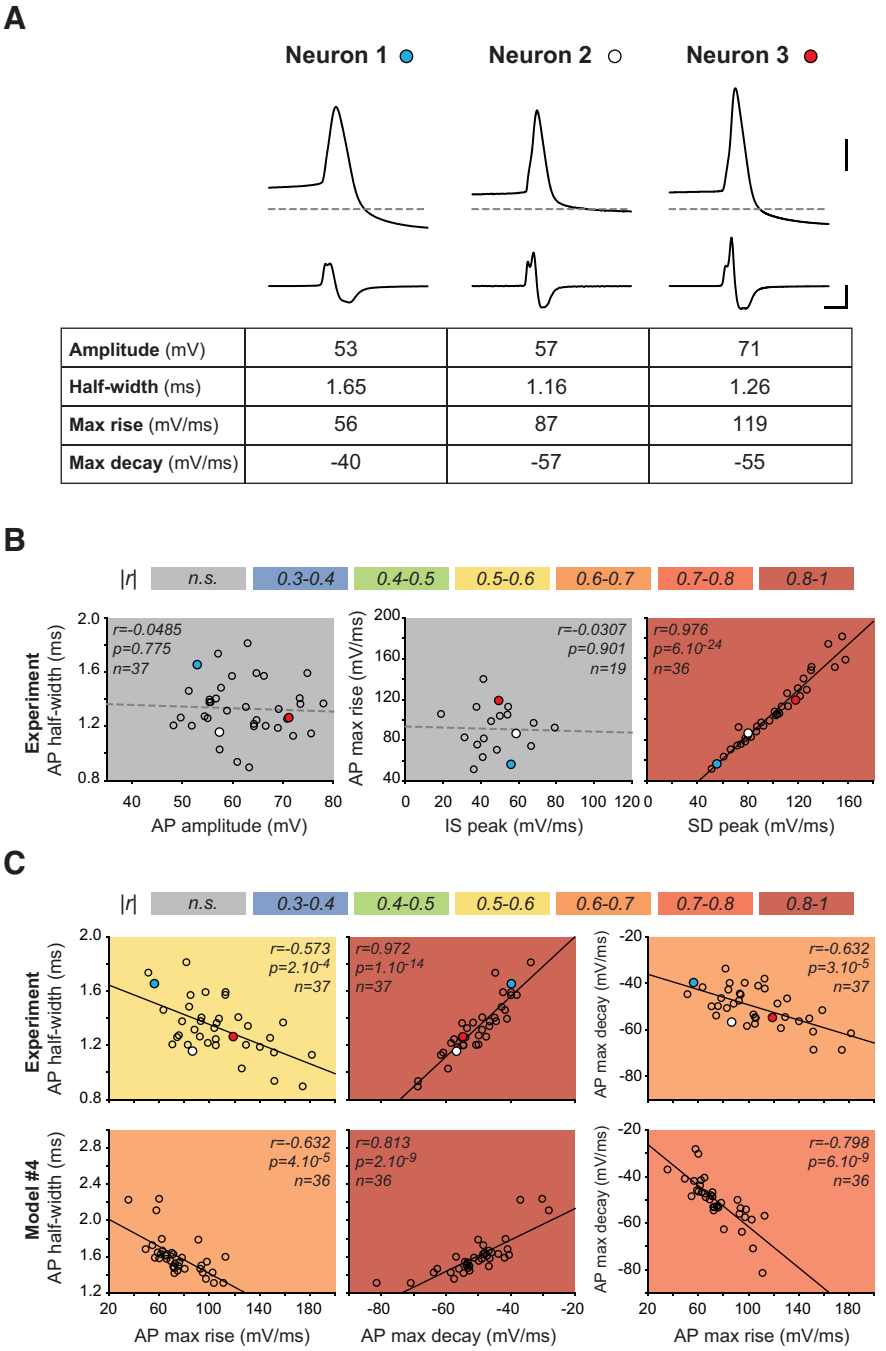

Amplitude (mV)	53	57	71
Half-width (ms)	1.65	1.16	1.26
Max rise (mV/ms)	56	87	119
Max decay (mV/ms)	-40	-57	-55

Figure 7. Cell-to-cell variations in AP half-width are mainly because of changes in AP decay rate. ***A***, Top, Example traces representing the voltage recording (top traces) and the voltage first derivative signal (bottom traces) for three neurons displaying different AP shapes. Bottom, Table represents the corresponding values of AP amplitude, half-width, maximum rise slope, and maximum decay slope. ***B***, Left, Scatter plots representing the relationships between AP half-width and AP amplitude (left), and AP maximum rise slope and the IS and SD components of the AP (middle and right) in real neurons. Gray dotted lines indicate nonsignificant correlations. Scatter plots are color-coded, depending on the value of the correlation coefficient. ***C***, Left, Middle, Scatter plots representing the relationships between AP half-width and AP maximum rise slope and maximum decay slope in the real neurons (top row) and in the heterogeneous model (bottom row). Right, Scatter plots representing the relationships between AP maximum decay slope and AP maximum rise slope in the same samples. Scatter plots are color-coded, depending on the value of the correlation coefficient. Blue, white, and red dots represent the specific values obtained for the three neurons presented in ***A***. Calibrations: ***A***, vertical 20 mV (top traces), 50 mV/ms (bottom traces), horizontal 2 ms.

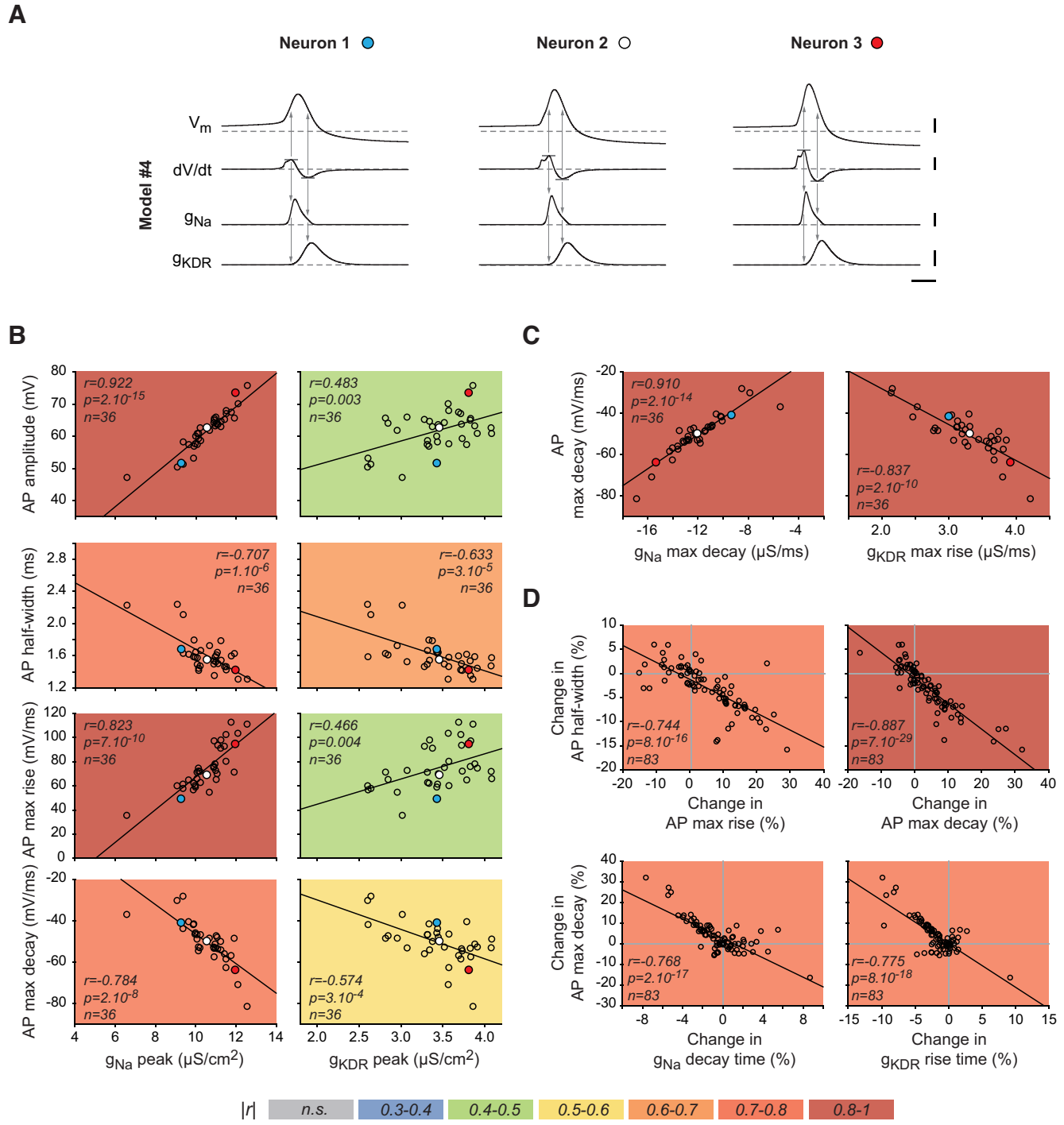

Figure 8. Variations in AP duration in the model are explained by variations in peak conductance and kinetics of sodium and delayed rectifier potassium conductances. ***A***, Example traces representing (from top to bottom) the voltage recording, the voltage first derivative signal, g_{Na} time course, and g_{KDR} time course for three model neurons displaying different AP durations. Horizontal gray bars are used to identify the maximum rise and decay slopes on the voltage derivative signal. Vertical arrows indicate the corresponding times on the other traces. ***B***, Scatter plots representing the relationships between AP properties (from top to bottom, amplitude, half-width, maximum rise slope, maximum decay slope) and g_{Na} or g_{KDR} peak conductances. Scatter plots are color-coded, depending on the value of the correlation coefficient. ***C***, Scatter plots representing the relationships between AP maximum decay slope and g_{Na} maximum decay or g_{KDR} maximum rise slopes. Scatter plots are color-coded, depending on the value of the correlation coefficient. ***D***, Top, Scatter plots representing the relationships between the dendrotomy-induced changes in AP half-width and the changes in AP maximum rise or decay slopes. Bottom, Scatter plots representing the relationships between the dendrotomy-induced changes in AP maximum decay and the changes in g_{Na} decay time or g_{KDR} rise time. Scatter plots are color-coded, depending on the value of the correlation coefficient. Blue, white, and red dots represent the specific values obtained for the three models presented in ***A***. Calibration: ***A***, vertical 20 mV (V_m), 50 mV/ms (dV/dt), 4µS/cm^2 (g_{Na}), 2µS/cm^2 (g_{KDR}), horizontal 2 ms. Horizontal dotted lines indicate −60 mV (Vm trace) or 0 (mV/ms or µS/cm^2).

neuronal types (Dufour et al., 2014). In contrast, one modeling study investigated specifically the influence of dendritic morphology on AP properties, focusing in particular on AP back-propagation in various neuronal types (Vetter et al., 2001). By comparing the back-propagating profiles in eight different cell types, the authors demonstrated that dendritic morphology imposes strong constraints on the density of dendritic sodium channels necessary to achieve faithful back-propagation: neurons with a relatively simple dendritic tree, such as SNc DA neurons, require a fairly low density of sodium channels while Purkinje

neurons never attain active dendritic AP propagation, even in the presence of a high sodium channel density (Vetter et al., 2001). More interestingly, these two cell types are less sensitive to changes in sodium channel density than most of the other neuronal types analyzed in the study (hippocampal and cortical interneurons and principal cells), which can display passive or active AP propagation depending on sodium channel density (Vetter et al., 2001). Our experimental and computational results extend these results by demonstrating that dendritic morphology also plays a critical role in defining the variation in AP shape across SNc DA neurons, despite substantial cell-to-cell variability in sodium channel density (Moubarak et al., 2019).

One may argue that the variability in ABD and nABD morphologies reported here is partly because of the slicing procedure, and that we may have overestimated the cell-to-cell variations in dendritic topology, because of artifactual sectioning of distal dendrites. While this may be true, the lack of a preferred orientation for the dendritic arborization of SNc DA neurons (Preston et al., 1981; Tepper et al., 1987; Lin et al., 2003) suggests that ABDs and nABDs should have been affected with an equiprobability. Based on our results, such artifactual distal dendrotomy would mainly increase the range of variation of both dendritic complexities and AP duration, thus favoring the detection of a correlation between these parameters. Be that as it may, there is no reason to think that artifactual dendritic sectioning could create the correlation observed between AP shape and dendritic topology, and the results of our computational modeling and dendrotomy experiments provide biophysical explanations for this relationship.

An intriguing finding of the current study is that the statistical dependence between dendritic topology and AP HW is only reproduced when heterogeneous densities of g_{Na} and g_{Ca} are implemented in the computational model. In contrast, the outside-out recordings obtained in a previous study (Moubarak et al., 2019) did not reveal statistical differences in sodium current density between the ABD and the nABDs. Unfortunately, although outside-out recordings are widely used to estimate current densities, this technique does not appear sufficiently accurate to reveal a heterogeneous density of g_{Na} in the dendrites of SNc DA neurons in the range suggested by the model. First, the method we used to determine the patch area, and thus the capacitance, was based on an approximately linear but highly scattered relationship between pipette resistance ant patch area (Sakmann and Neher, 1995). Second, ion currents in DA neurons display a significant variability from neuron to neuron (Liss et al., 2001; Gentet and Williams, 2007; Seutin and Engel, 2010; Amendola et al., 2012; Engel and Seutin, 2015; Moubarak et al., 2019; Haddjeri-Hopkins et al., 2021) that would obscure the presence of subcellular heterogeneity when comparing g_{Na} between the ABD and nABDs in different neurons. In these conditions, increasing the number of recordings and the accuracy of patch surface area estimation (e.g., using elastomer microspheres to measure patch capacitance) (see Sakmann and Neher, 1995) would be needed to improve the statistical power of g_{Na} comparison and reveal a heterogeneous density between the ABD and nABDs. In order to be consistent with our previous experimental results (Moubarak et al., 2019), we nonetheless tested the possibility that g_{Na} and g_{Ca} could be homogeneous within a same neuron but scale with ABD length across neurons (data not shown). While this manipulation reproduced the correlations between AP HW and dendritic topology, it failed to reproduce the opposite influences of ABD and nABD dendrotomies. On the other hand, increasing the excitability of the ABD compared with the nABDs by increasing g_H or decreasing g_K in the ABD failed to reproduce the correlation between AP HW and dendritic topology (Fig. 4*B*,*C*), which necessitated specifically an increase in g_{Na} and/or g_{Ca}. In conclusion, a slightly heterogeneous density of g_{Na} and g_{Ca} seems to be the simplest explanation of why ABD and nABDs have an opposite influence on AP HW.

The investigation of the biophysical mechanisms performed on the experimental data revealed that most changes in AP half-width seem to be because of changes in AP decay rate, a relationship mimicked by both versions of our model. This may seem surprising since sodium currents are supposed to mainly define the rising phase of the AP (Hille, 2001; Bean, 2007). Even more surprisingly, although delayed rectifier currents are critical for defining the decaying phase of the AP (Hille, 2001; Bean, 2007; Kimm et al., 2015), decreasing the delayed rectifier conductance in the ABD did not reproduce the relationship between morphology and AP half-width (Fig. 4). However, the analyses performed on the model suggested that the sodium conductance may have a very strong influence on both the rising and decaying phases of the AP. First, g_{Na} peak conductance displayed stronger correlations with AP properties (amplitude, half-width, rise slope, decay slope) than g_{KDR}. The analysis of the kinetics of both conductances then showed that the decaying phase of g_{Na} and the rising phase of g_{KDR} are the best predictors of AP decay rate, for both cell-to-cell variations and dendrotomy-induced changes in AP half-width. Interestingly, as mentioned before, while g_{Na} kinetics were strongly correlated with g_{Na} peak conductance, g_{KDR} rise time was not correlated with g_{KDR} peak conductance but with g_{Na} kinetics. This effect was also seen in the dendrotomy simulation, where changes in g_{KDR} rise time were not predicted by changes in g_{KDR} peak conductance but predicted by changes in g_{Na} kinetics ($r > 0.8$). In the light of these results, we hypothesize that the effective g_{Na} conductance underlying the SD component of the AP will vary depending on the complexity/length of the ABD, such that the AP recorded at the soma and dominated by the ABD contribution will be mainly defined by ABD complexity. In this context, the AP initiated at the AIS triggers an AP in the ABD and adjacent dendrites, leading to a larger effective g_{Na} conductance that speeds up g_{Na} kinetics (rise and decay) and in turns allows for a faster activation of g_{KDR} (rise time), the combined variations of g_{Na} decay time and g_{KDR} rise time leading to strong variations in SD AP decay slope.

One important difference between our model and the real SNc DA neurons is the absence in the model of BKCa potassium channels, which have been demonstrated to play a central role in controlling AP half-width. As suggested by Kimm et al. (2015), both Kv2 (delayed rectifier) and BKCa potassium currents control AP half-width by setting the repolarization rate. In particular, the selective blockade of BK channels with iberiotoxin leads to a 50% increase in AP half-width. Thus, the role played by the g_{KDR} conductance in our model may strongly rely on BK channels in real SNc DA neurons. Nonetheless, the ability of our heterogeneous model to reproduce the relationships between morphology and AP half-width suggests that the recruitment of repolarizing currents (including BK channels) in the ABD strongly depends on the effective conductance and kinetics of the SD sodium conductance, an effect that is exacerbated by a higher density of sodium channels in the ABD.

In conclusion, the current study and our previous work (Moubarak et al., 2019) highlight the importance of SD excitability in SNc DA neurons, and suggest that the sodium channels expressed in particular in the axon-bearing dendrite not only

play a central role in setting pacemaking frequency but also define the precise kinetics and shape of the back-propagating APs.

References

Alle H, Kubota H, Geiger JR (2011) Sparse but highly efficient Kv3 outpace BKCa channels in action potential repolarization at hippocampal mossy fiber boutons. J Neurosci 31:8001–8012.

Alle H, Roth A, Geiger JR (2009) Energy-efficient action potentials in hippocampal mossy fibers. Science 325:1405–1408.

Amendola J, Woodhouse A, Martin-Eauclaire MF, Goaillard JM (2012) Ca(2)(+)/cAMP-sensitive covariation of I(A) and I(H) voltage dependences tunes rebound firing in dopaminergic neurons. J Neurosci 32:2166–2181.

Bean BP (2007) The action potential in mammalian central neurons. Nat Rev Neurosci 8:451–465.

Benjamini Y, Hochberg Y (1995) Controlling the false discovery rate: a practical and powerful approach to multiple testing. J R Stat Soc B 57:289–300.

Brette R (2013) Sharpness of spike initiation in neurons explained by compartmentalization. PLoS Comput Biol 9:e1003338.

Bucher D, Goaillard JM (2011) Beyond faithful conduction: short-term dynamics, neuromodulation, and long-term regulation of spike propagation in the axon. Prog Neurobiol 94:307–346.

Carnevale NT, Hines ML (2005) The NEURON book, p 479. Cambridge: Cambridge UP.

Carter BC, Bean BP (2009) Sodium entry during action potentials of mammalian neurons: incomplete inactivation and reduced metabolic efficiency in fast-spiking neurons. Neuron 64:898–909.

Carter BC, Bean BP (2011) Incomplete inactivation and rapid recovery of voltage-dependent sodium channels during high-frequency firing in cerebellar Purkinje neurons. J Neurophysiol 105:860–871.

Delvendahl I, Hallermann S (2016) The cerebellar mossy fiber synapse as a model for high-frequency transmission in the mammalian CNS. Trends Neurosci 39:722–737.

Destexhe A, Babloyantz A, Sejnowski TJ (1993) Ionic mechanisms for intrinsic slow oscillations in thalamic relay neurons. Biophys J 65:1538–1552.

Ding S, Wei W, Zhou FM (2011) Molecular and functional differences in voltage-activated sodium currents between GABA projection neurons and dopamine neurons in the substantia nigra. J Neurophysiol 106:3019–3034.

Dufour MA, Woodhouse A, Amendola J, Goaillard JM (2014) Non-linear developmental trajectory of electrical phenotype in rat substantia nigra pars compacta dopaminergic neurons. Elife 3:e04059.

Engel D, Seutin V (2015) High dendritic expression of Ih in the proximity of the axon origin controls the integrative properties of nigral dopamine neurons. J Physiol 593:4905–4922.

Eyal G, Mansvelder HD, de Kock CP, Segev I (2014) Dendrites impact the encoding capabilities of the axon. J Neurosci 34:8063–8071.

Geiger JR, Jonas P (2000) Dynamic control of presynaptic Ca(2+) inflow by fast-inactivating K(+) channels in hippocampal mossy fiber boutons. Neuron 28:927–939.

Gentet LJ, Williams SR (2007) Dopamine gates action potential backpropagation in midbrain dopaminergic neurons. J Neurosci 27:1892–1901.

Go MA, Choy JM, Colibaba AS, Redman S, Bachor HA, Stricker C, Daria VR (2016) Targeted pruning of a neuron's dendritic tree via femtosecond laser dendrotomy. Sci Rep 6:19078.

Goaillard JM, Moubarak E, Tapia M, Tell F (2020) Diversity of axonal and dendritic contributions to neuronal output. Front Cell Neurosci 13:570.

Gonzalez-Cabrera C, Meza R, Ulloa L, Merino-Sepulveda P, Luco V, Sanhueza A, Onate-Ponce A, Bolam JP, Henny P (2017) Characterization of the axon initial segment of mice substantia nigra dopaminergic neurons. J Comp Neurol 525:3529–3542.

Gulledge AT, Bravo JJ (2016) Neuron morphology influences axon initial segment plasticity. eNeuro 3:ENEURO.0085-15.2016.

Haddjeri-Hopkins A, Tapia M, Ramirez-Franco J, Tell F, Marqueze-Pouey B, Amalric M, Goaillard JM (2021) Refining the identity and role of Kv4 channels in mouse substantia nigra dopaminergic neurons. eNeuro 8:ENEURO.0207-21.2021.

Hausser M, Stuart G, Racca C, Sakmann B (1995) Axonal initiation and active dendritic propagation of action potentials in substantia nigra neurons. Neuron 15:637–647.

Hille B (2001) Ion channels of excitable membranes, Ed 3. Sunderland, MA: Sinauer.

Hines ML, Carnevale NT (1997) The NEURON simulation environment. Neural Comput 9:1179–1209.

Hines ML, Carnevale NT (2001) NEURON: a tool for neuroscientists. Neuroscientist 7:123–135.

Hu W, Tian C, Li T, Yang M, Hou H, Shu Y (2009) Distinct contributions of Na(v)1.6 and Na(v)1.2 in action potential initiation and backpropagation. Nat Neurosci 12:996–1002.

Hunsberger MS, Mynlieff M (2020) BK potassium currents contribute differently to action potential waveform and firing rate as rat hippocampal neurons mature in the first postnatal week. J Neurophysiol 124:703–714.

Jang J, Bumum K, Jang M, Kim SH, Cho H, Chung S, Kim HJ, Park MK (2014) Balance between the proximal dendritic compartment and the soma determines spontaneous firing rate in midbrain dopamine neurons. J Physiol 592:2829–2844.

Kaczmarek LK, Zhang Y (2017) Kv3 channels: enablers of rapid firing, neurotransmitter release, and neuronal endurance. Physiol Rev 97:1431–1468.

Kimm T, Khaliq ZM, Bean BP (2015) Differential regulation of action potential shape and burst-frequency firing by BK and Kv2 channels in substantia nigra dopaminergic neurons. J Neurosci 35:16404–16417.

Kole MH, Brette R (2018) The electrical significance of axon location diversity. Curr Opin Neurobiol 51:52–59.

Kole MH, Ilschner SU, Kampa BM, Williams SR, Ruben PC, Stuart GJ (2008) Action potential generation requires a high sodium channel density in the axon initial segment. Nat Neurosci 11:178–186.

Kuba H, Yamada R, Fukui I, Ohmori H (2005) Tonotopic specialization of auditory coincidence detection in nucleus laminaris of the chick. J Neurosci 25:1924–1934.

Kuhn M (2021) caret: classification and regression training. R package version 6.0-88.

Lien CC, Jonas P (2003) Kv3 potassium conductance is necessary and kinetically optimized for high-frequency action potential generation in hippocampal interneurons. J Neurosci 23:2058–2068.

Lin JY, van Wyk M, Bowala TK, Teo MY, Lipski J (2003) Dendritic projections and dye-coupling in dopaminergic neurons of the substantia nigra examined in horizontal brain slices from young rats. J Neurophysiol 90:2531–2535.

Liss B, Franz O, Sewing S, Bruns R, Neuhoff H, Roeper J (2001) Tuning pacemaker frequency of individual dopaminergic neurons by Kv4.3L and KChip3.1 transcription. EMBO J 20:5715–5724.

Longair MH, Baker DA, Armstrong JD (2011) Simple Neurite Tracer: open source software for reconstruction, visualization and analysis of neuronal processes. Bioinformatics 27:2453–2454.

Ma MH, Koester J (1996) The role of K^+ currents in frequency-dependent spike broadening in Aplysia R20 neurons: a dynamic-clamp analysis. J Neurosci 16:4089–4101.

Meza RC, Lopez-Jury L, Canavier CC, Henny P (2018) Role of the axon initial segment in the control of spontaneous frequency of nigral dopaminergic neurons in vivo. J Neurosci 38:733–744.

Migliore M, Cannia C, Canavier CC (2008) A modeling study suggesting a possible pharmacological target to mitigate the effects of ethanol on reward-related dopaminergic signaling. J Neurophysiol 99:2703–2707.

Moubarak E, Engel D, Dufour MA, Tapia M, Tell F, Goaillard JM (2019) Robustness to axon initial segment variation is explained by somatodendritic excitability in rat substantia nigra dopaminergic neurons. J Neurosci 39:5044–5063.

Philippart F, Destreel G, Merino-Sepulveda P, Henny P, Engel D, Seutin V (2016) Differential somatic Ca^{2+} channel profile in midbrain dopaminergic neurons. J Neurosci 36:7234–7245.

Preston RJ, McCrea RA, Chang HT, Kitai ST (1981) Anatomy and physiology of substantia nigra and retrorubral neurons studied by extra- and intracellular recording and by horseradish peroxidase labeling. Neuroscience 6:331–344.

Puopolo M, Raviola E, Bean BP (2007) Roles of subthreshold calcium current and sodium current in spontaneous firing of mouse midbrain dopamine neurons. J Neurosci 27:645–656.

Rama S, Zbili M, Fekete A, Tapia M, Benitez MJ, Boumedine N, Garrido JJ, Debanne D (2017) The role of axonal Kv1 channels in CA3 pyramidal cell excitability. Sci Rep 7:315.

R Core Team (2020) R: a language and environment for statistical computing. Vienna: R Foundation for Statistical Computing.

Rousselet GA, Pernet CR, Wilcox RR (2021) The percentile bootstrap: a primer with step-by-step instructions in R. Adv Meth Pract Psych 4:1–10.

Rudy B, McBain CJ (2001) Kv3 channels: voltage-gated K^+ channels designed for high-frequency repetitive firing. Trends Neurosci 24:517–526.

Rueden CT, Schindelin J, Hiner MC, DeZonia BE, Walter AE, Arena ET, Eliceiri KW (2017) ImageJ2: imageJ for the next generation of scientific image data. BMC Bioinformatics 18:529.

Sakmann B, Neher E (1995) Single-channel recording, Ed 2. New York: Plenum.

Sanchez-Aguilera A, Monedero G, Colino A, Vicente-Torres MA (2020) Development of action potential waveform in hippocampal CA1 pyramidal neurons. Neuroscience 442:151–167.

Schild JH, Khushalani S, Clark JW, Andresen MC, Kunze DL, Yang M (1993) An ionic current model for neurons in the rat medial nucleus tractus solitarii receiving sensory afferent input. J Physiol 469:341–363.

Schindelin J, Arganda-Carreras I, Frise E, Kaynig V, Longair M, Pietzsch T, Preibisch S, Rueden C, Saalfeld S, Schmid B, Tinevez JY, White DJ, Hartenstein V, Eliceiri K, Tomancak P, Cardona A (2012) Fiji: an open-source platform for biological-image analysis. Nat Methods 9:676–682.

Schneider CA, Rasband WS, Eliceiri KW (2012) NIH Image to ImageJ: 25 years of image analysis. Nat Methods 9:671–675.

Sengupta B, Stemmler M, Laughlin SB, Niven JE (2010) Action potential energy efficiency varies among neuron types in vertebrates and invertebrates. PLoS Comput Biol 6:e1000840.

Seutin V, Engel D (2010) Differences in Na^+ conductance density and Na^+ channel functional properties between dopamine and GABA neurons of the rat substantia nigra. J Neurophysiol 103:3099–3114.

Tepper JM, Sawyer SF, Groves PM (1987) Electrophysiologically identified nigral dopaminergic neurons intracellularly labeled with HRP: light-microscopic analysis. J Neurosci 7:2794–2806.

Tucker KR, Huertas MA, Horn JP, Canavier CC, Levitan ES (2012) Pacemaker rate and depolarization block in nigral dopamine neurons: a somatic sodium channel balancing act. J Neurosci 32:14519–14531.

Vetter P, Roth A, Hausser M (2001) Propagation of action potentials in dendrites depends on dendritic morphology. J Neurophysiol 85:926–937.

Wilson CJ, Callaway JC (2000) Coupled oscillator model of the dopaminergic neuron of the substantia nigra. J Neurophysiol 83:3084–3100.

Zhou D, Lambert S, Malen PL, Carpenter S, Boland LM, Bennett V (1998) AnkyrinG is required for clustering of voltage-gated Na channels at axon initial segments and for normal action potential firing. J Cell Biol 143:1295–1304.